


Observation of Pairwise Level Degeneracies and the Quantum Regime of the Arrhenius Law in a Double-Well Parametric Oscillator

Nicholas E. Frattini¹,^{*}†, Rodrigo G. Cortiñas¹,^{*}‡, Jayameenakshi Venkatraman¹, Xu Xiao, Qile Su, Chan U. Lei¹, Benjamin J. Chapman¹, Vidul R. Joshi, S. M. Girvin¹, Robert J. Schoelkopf, Shruti Puri, and Michel H. Devoret¹§
Department of Applied Physics and Physics, Yale University, New Haven, Connecticut 06520, USA

 (Received 28 December 2022; revised 18 May 2024; accepted 9 July 2024; published 3 September 2024)

By applying a microwave drive to a specially designed Josephson circuit, we have realized a double-well model system: a Kerr oscillator submitted to a squeezing force. We have observed, for the first time, the spectroscopic fingerprint of a quantum double-well Hamiltonian when its barrier height is increased: a pairwise level kissing (coalescence) corresponding to the exponential reduction of tunnel splitting in the excited states as they sink under the barrier. The discrete levels in the wells also manifest themselves in the activation time across the barrier which, instead of increasing smoothly as a function of the barrier height, presents steps each time a pair of excited states is captured by the wells. This experiment illustrates the quantum regime of Arrhenius's law, whose observation is made possible here by the unprecedented combination of low dissipation, time-resolved state control, 98.5% quantum nondemolition single shot measurement fidelity, and complete microwave control over all Hamiltonian parameters in the quantum regime. Direct applications to quantum computation and simulation are discussed.

DOI: [10.1103/PhysRevX.14.031040](https://doi.org/10.1103/PhysRevX.14.031040)

Subject Areas: Quantum Physics, Quantum Information

I. INTRODUCTION

Quantum tunneling under the barrier of a double-well potential is a standard textbook effect illustrating the characteristics of quantum physics in a system with a direct classical counterpart [1]. Since its discovery in the early days of quantum theory [2], the effect has been observed in a variety of natural [2–6] and synthetic [7–24] systems. However, preparing excited states in a double-well potential is difficult and controlling the Hamiltonian parameters can be challenging. As a consequence, studies of tunneling have usually been restricted to the energy splitting and dynamics of the ground and first excited states [25–30]. The higher excited states, though, crucially influence activation over the barrier [29], which provides a minimal model for many molecular and nuclear reactions.

In superconducting circuits, a prototypical double-well system has long been available in the form of the flux qubit [31,32] and its cousin the rf SQUID [33–35], each interrogated with a variety of spectroscopic techniques [36,37].

The advent of tunable tunneling barrier heights [35,38–40] makes these qubits particularly appealing for quantum annealing applications [41]. The role of excited states has been utilized, for example, in Mach-Zehnder interferometry [42], yet the spectroscopic measurement of the excited states as the tunnel barrier is finely tuned in this and other systems has remained elusive, in part due to insufficient coherence, precision control, and readout fidelity.

In this work, we realize a fully controllable double-well Hamiltonian in a strongly microwave-driven superconducting circuit and observe elementary predictions of quantum mechanics not accessed before. Assisted by precision measurement techniques, we observe the exponential reduction of tunneling with barrier height for several excited states, an effect we refer to in this work as *spectral kissing* (see below). We also uncover how the quantization of action modifies the Arrhenius's law, governing thermal activation across the barrier [27,43–47]. Apart from this demonstration of microscopic kinetic rate theory, our experimental system implements a Kerr-cat qubit [48] that attains record relaxation times. We achieve a bit-flip rate 1450 times smaller than the phase-flip rate while remaining quantum coherent enough for gate operations and high-fidelity measurements. This leaves our system poised for potential applications in quantum computing [49–54].

^{*}These authors contributed equally to this work.

†Contact author: nick@nordquantique.ca

‡Contact author: rodrigo.cortinas@yale.edu

§Contact author: michel.devoret@yale.edu

Published by the American Physical Society under the terms of the Creative Commons Attribution 4.0 International license. Further distribution of this work must maintain attribution to the author(s) and the published article's title, journal citation, and DOI.

II. MODEL SYSTEM

Our experiment is performed in a strongly microwave-driven superconducting Kerr parametric oscillator [55]

operating in the quantum regime. The central element of the circuit is the Josephson tunnel junction, which is the exact electrical analog of a pendulum [56]. We combine several Josephson junctions in an array of two superconducting nonlinear asymmetric inductive elements (SNAILs) [57–59], which creates the analog of an asymmetric pendulum with a third-order nonlinearity, or in other words, a system capable of three-wave mixing. The Hamiltonian for this so-called SNAIL transmon, when driven via its charge degree of freedom, reads

$$\hat{H}(t)/\hbar = \omega_o \hat{a}^\dagger \hat{a} + \sum_{m=3}^{\infty} \frac{g_m}{m} (\hat{a} + \hat{a}^\dagger)^m - i\Omega_d (\hat{a} - \hat{a}^\dagger) \cos \omega_d t, \quad (1)$$

which, in turn, describes a generic driven nonlinear oscillator. In this expression, \hat{a} is the bosonic annihilation operator. The parameters ω_o and $g_m \ll \omega_o$ are the bare oscillator frequency and the m th-order nonlinearity coefficients of the oscillator. The sinusoidal drive is specified by its amplitude Ω_d and frequency ω_d .

When the drive frequency approaches twice the natural oscillator frequency $\omega_d \approx 2\omega_o$, the system governed by Eq. (1) exhibits a period-doubling bifurcation whose ground states, in the quantum regime, host the Kerr-cat qubit [48], one representative of *stabilized* Schrödinger cat qubits [60–64]. After a canonical transformation and keeping terms beyond leading order in the rotating wave approximation (RWA) (see Appendix A and Ref. [65]), the evolution in the frame rotating at $\omega_d/2$ is given by the effective, time-independent, squeeze-driven Kerr Hamiltonian:

$$\hat{H}_{\text{SK}}/\hbar = \epsilon_2 (\hat{a}^{\dagger 2} + \hat{a}^2) - K \hat{a}^{\dagger 2} \hat{a}^2. \quad (2)$$

Concretely, the drive frequency chosen for Eq. (2) to be valid is $\omega_d = 2\omega_a$, where $\omega_a = \omega_o + 3g_4 - 20g_3^2/3\omega_o + (6g_4 - 9g_3^2/\omega_o)(2\Omega_d/3\omega_o)^2$ is the Lamb- and Stark-shifted small oscillation frequency. The quartic Kerr nonlinearity is given to leading order by $K = -(3g_4/2) + (10g_3^2/3\omega_o)$. The quadratic term in Eq. (2) conserves the photon-number parity—but not the photon number—and is governed by the squeezing amplitude $\epsilon_2 = g_3(2\Omega_d/3\omega_o)$. Both the effective Kerr coefficient and the squeezing amplitude are functions of the bare nonlinearities and the drive parameters. Note that the Hamiltonian describes a double-well system. The barrier height is given by $\hbar\epsilon_2^2/K$, and the interwell separation by $2\sqrt{\epsilon_2/K}$. Both can be controlled via the microwave drive amplitude and the Kerr nonlinearity, which itself depends on the applied magnetic field.

The quantum Hamiltonian in Eq. (2) has received theoretical attention over the previous decades [66–76] and, in particular, recently [77–86]. However, experiments

that adhere to this simple model require a Kerr nonlinear frequency shift much larger than the dissipation rate that is difficult to achieve, even in the classical regime. For systems with sizable dissipation, the stabilization of the associated period-doubled bifurcation is provided by losses and pump depletion, not by the Kerr nonlinearity. Alternatively, for systems where the nonlinearity dominates, spurious nonlinearities easily turn this strongly driven system into a chaotic one. The experimental realization of a system described by Eq. (2), in a fully controllable quantum regime and including excited states, is important in view of recent proposals for quantum information processing with driven circuits [49–54,75,87].

III. EXPERIMENT AND RESULTS

The setup is presented in Figs. 1(a)–1(c) where we show our SNAIL circuit. The array of SNAILs, flux biased at $\Phi/\Phi_0 = 0.33$ via current applied to coils beneath the copper section of the package, provides the target parameters of resonance frequency $\omega_a/2\pi = 6.03$ GHz and Kerr nonlinearity $K/2\pi = 320$ kHz. In absence of squeezing drive, this SNAIL transmon has an excitation lifetime of $T_1 = (20 \pm 3)$ μs , and the superposition lifetime of its two lowest lying Fock states is $T_{2\text{R}} = (2.17 \pm 0.05)$ μs .

In Fig. 1(d), we show the Wigner phase-space representation $H_{\text{SK}}(a, a^*)$ [89,90] of \hat{H}_{SK} , which we also refer to as the *metapotential* of the system [71]. The metapotential provides benefits for intuition in that it is a representation of the effective time-independent Hamiltonian of the driven system. Its coordinates a (a^*) are the same as those of the Wigner function, namely, the Wigner transform of the bosonic annihilation (creation) operators \hat{a} (\hat{a}^\dagger). The Wigner functions of the seven lowest lying energy states in the phase-space Hamiltonian surface (gray) are also plotted. The ground state of the system is doubly degenerate and spanned by the even and odd Schrödinger cat states $|\mathcal{C}_\alpha^\pm\rangle \propto |\pm\alpha\rangle \pm |-\alpha\rangle$, where $|\pm\alpha\rangle$ are coherent states with squared amplitude $|\alpha|^2 = \epsilon_2/K$. We refer to these ground states as the Kerr-cat qubit computational states $|\pm Z\rangle = |\mathcal{C}_\alpha^\pm\rangle$ with Wigner functions shown in Fig. 1(e) for $|\alpha|^2 = 8.5$. Their equal weight superpositions $|\pm X\rangle = |\pm\alpha\rangle + \mathcal{O}(e^{-2|\alpha|^2})$ correspond, in the lab frame, to two oscillations of the circuit with a relative phase shift of 180° .

Measurements of the oscillator state were performed through a separate on-chip readout resonator with frequency $\omega_b/2\pi = 8.5$ GHz and coupling rate $\kappa_b/2\pi = 0.40$ MHz to the quantum-limited measurement chain (see other parameters of the setup in Table II in Appendix C). In order to activate a frequency-converting beam-splitter interaction between the squeeze-driven Kerr oscillator and the readout resonator, we apply an additional drive at $\omega_{\text{BS}} = \omega_b - \omega_d/2$. This transfers photons from the squeeze-driven Kerr oscillator to the readout resonator, which are subsequently collected by the measurement

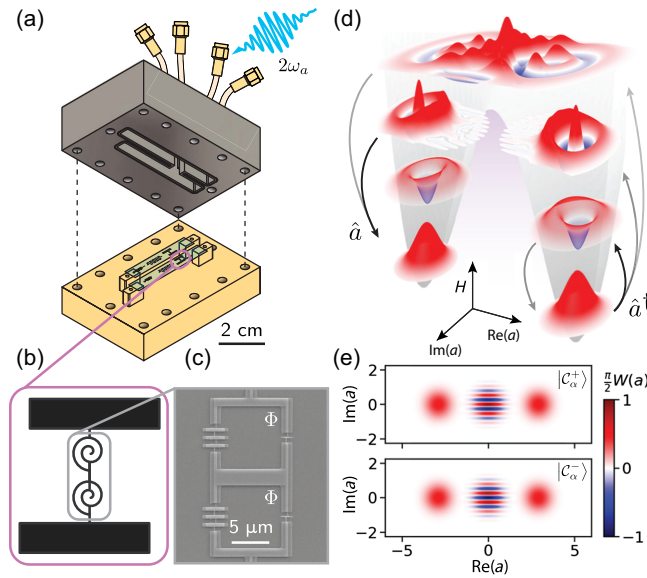


FIG. 1. Implementation of the squeeze-driven Kerr oscillator. (a) Rendering of the half-aluminum, half-copper sample package containing two sapphire chips, each with a SNAIL transmon, readout resonator, and Purcell filter (see Ref. [88]). Only one chip is used in the present work. Applying a strong microwave drive at $\omega_d \approx 2\omega_a$ transforms the SNAIL-transmon Hamiltonian into a squeeze-driven Kerr oscillator. (b) Schematic of the SNAIL transmon: A two-SNAIL array serves as the nonlinear element. The capacitor pads are shifted with respect to the axis of the array to couple it to the readout resonator. (c) Scanning electron micrograph of the two-SNAIL array. The SNAIL loops are biased with an external magnetic flux $\Phi/\Phi_0 = 0.33$, where Φ_0 is the magnetic flux quantum. (d) Metapotential (gray) of the squeeze-driven Kerr oscillator static-effective Hamiltonian Eq. (2) for $\epsilon_2/K = 8.5$. Wigner functions of the first seven eigenstates are shown. The highly nonlinear double-well structure hosts three pairs of degenerate eigenstates. The arrows represent incoherent jumps causing a well-occupation flip from right to left. (e) Wigner functions of the even and odd superpositions of the two degenerate ground coherent states of (d), the Kerr-cat qubit $|\pm Z\rangle = |c_{\alpha}^{\pm}\rangle$ states.

chain. The strong squeezing drive ($\epsilon_2 > K$) replenishes these radiated photons, thereby maintaining a steady oscillation amplitude. This is a necessary condition for a quantum nondemolition (QND) measurement of the *which-well* observable $\hat{X} \approx |+\alpha\rangle\langle +\alpha| - |-\alpha\rangle\langle -\alpha|$ [48]. In effect, the readout resonator state is displaced, conditioned on which of the two metapotential wells is occupied.

In Fig. 2(a), we show a histogram of \hat{X} measurements. The single shot readout infidelity is 0.46%. Correlation measurements determined that the QND infidelity in our experiment is 1.5% (see Appendix D). These values mean that we can continuously monitor our system and reconstruct the trajectories associated with the quantum jumps of the well occupation.

In Fig. 2(b), we show the experimental protocol for measuring the quantum trajectories. After the squeezing

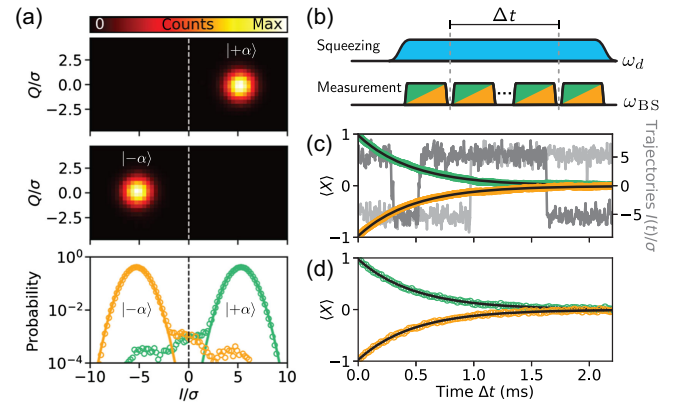


FIG. 2. QND measurement and quantum jumps. (a) Top and middle: histogram of the readout resonator output field when performing 2.5×10^8 measurements after preparation in $|\pm\alpha\rangle$ with a previous, stringently thresholded measurement with a bias of 6.5 standard deviations (σ). Bottom: corresponding probability distribution along the I quadrature, and Gaussian fits (solid lines) with standard deviation used to scale the axes. Applying a fair (unbiased) threshold represented by the dashed vertical line yields a readout infidelity of 0.46%. All data shown here are for $\epsilon_2/K = 10.7$. (b) Pulse sequence to performing repeated measurements, each with a duration of 4.44 μs . (c) Example quantum jump trajectories (gray) under repeated measurements. Averages of trajectories conditioned on the first measurement of $|\pm\alpha\rangle$ (green and orange) fit together with single exponentials (black line) with decay time $T_X^{\text{jumps}} = (485 \pm 1) \mu\text{s}$. (d) State lifetime for $|\pm\alpha\rangle$ (green and orange) with no intermediate measurements (free decay). Black lines are a single-exponential fit with decay time $T_X = (482 \pm 4) \mu\text{s}$.

drive is turned on, a waiting time equal to $5T_1$ is imposed to let the system adopt a steady state [91], and a series of measurements is then performed. The sequence of their outcomes constitutes a quantum trajectory record. Two examples of quantum trajectories are shown in shades of gray in Fig. 2(c). The green and orange data points correspond to averages of 5×10^5 trajectories, each conditioned on the initial measurement falling on the positive or negative side of a threshold defined by the demodulated field quadrature $I = 0$. The decay curve is fitted by a single exponential (black), yielding an incoherent environment-induced activation time of $T_{\pm X}^{\text{jumps}} = (485 \pm 1) \mu\text{s}$. We next compare these measurements to the free decay of the coherent states $|\pm\alpha\rangle$. This is obtained by performing only two measurements spaced by a variable idling time, in absence of continuous monitoring; the results are shown in Fig. 2(d). The decay is also fitted by an exponential whose lifetime is found to be $T_{\pm X} = (482 \pm 4) \mu\text{s}$, thus showing that continuous monitoring does not significantly modify the coherent state timescale T_X in the metapotential.

To observe the energy levels' dependence on the barrier height [74], we perform spectroscopy of discrete quantum energy levels as a function of the squeezing amplitude. This is achieved by interrupting the idling time, now kept

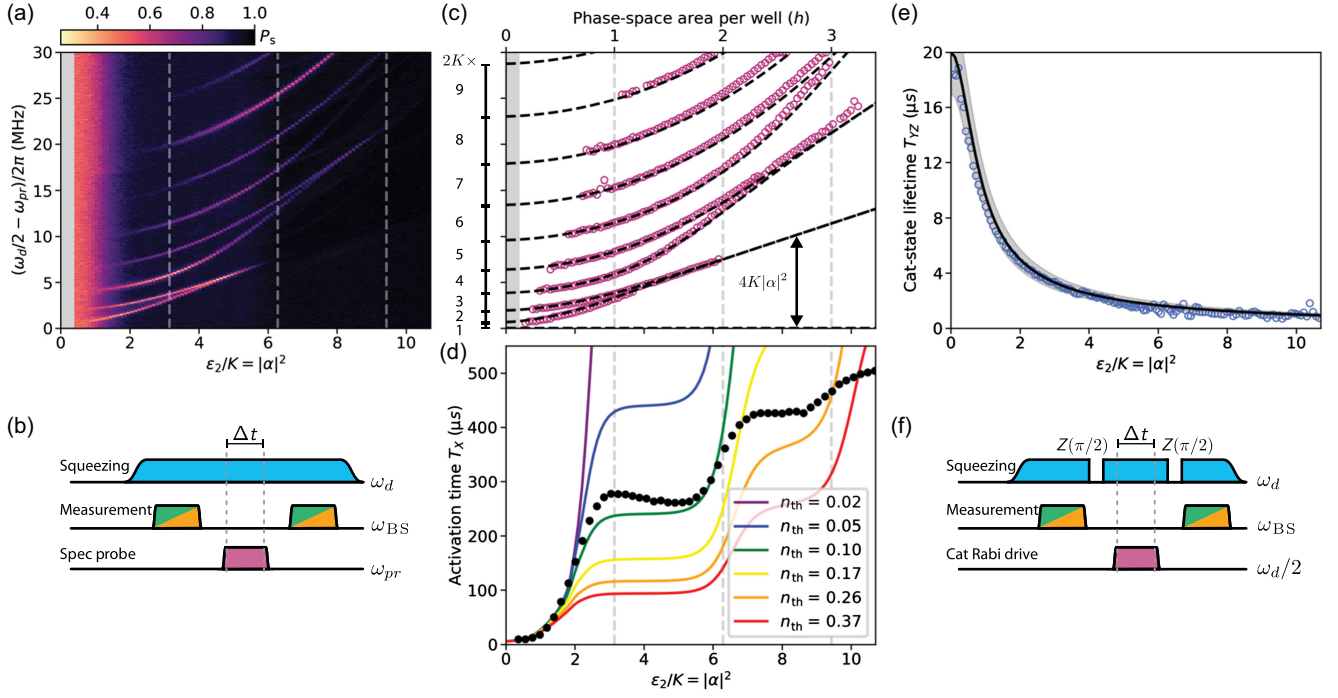


FIG. 3. Spectroscopic fingerprint of the squeeze-driven Kerr oscillator and coherence of the ground-state manifold. (a) Spectroscopy data taken with the pulse sequence in (b). While applying a squeezing drive with swept amplitude $\epsilon_2/K (= |\alpha|^2)$, we perform spectroscopy by scanning ω_{pr} . Color denotes probability P_s that both measurements give the same result. A low P_s means a transition has occurred between the readout pulses. For $|\alpha|^2 < 0.3$, the measurement is not QND and thus yields a poor contrast. (c) Purple open dots are the extracted resonances from (a). Black dashed lines are a parameter-free diagonalization of $-\hat{H}_{SK}$. Gray vertical lines indicate the number of levels per Hamiltonian well using quantization calculated by phase-space area (see Appendix F). (d) Coherent state lifetime T_X (black circles) as a function of squeezing amplitude, measured by fitted single-exponential decay timescale from experimental pulse sequences in (b) (without spectroscopy probe). Solid lines are extracted from fits to time-dependent master equation simulations including phenomenological parameters that emulate coupling to a photon bath at rate κ_1 with nonzero temperature n_{th} (colors), and low-frequency detuning noise (see Appendix G). (e) The cat-state—equally weighted superpositions of $|\pm\alpha\rangle$ —lifetime (T_{YZ} , blue open dots) as a function of its size ($|\alpha|^2$), measured with the Ramsey-like pulse sequence in (f). The solid line inside the gray band is the prediction with no free parameters.

constant, between the readout pulses by a microwave probe tone at frequency ω_{pr} . If ω_{pr} coincides with the energy difference between the ground state and an excited state close to or above the metapotential barrier, an interwell transition becomes likely. In Figures 3(a) and 3(b), we show the measurement of the survival probability P_s for an initial state localized in one well as a function of squeezing amplitude ϵ_2/K and probe frequency ω_{pr} . In Fig. 3(c), we show the fitted location of the spectroscopic lines as open purple dots. In the same figure, with dashed lines, we also show a numerical diagonalization with no adjustable parameters of the static-effective Hamiltonian Eq. (2). The agreement between theory and experiment is remarkable given the simplicity of the model. For $|\alpha|^2 \rightarrow 0$, we extrapolate the spectrum to that of the bare SNAIL transmon exhibiting the expected Kerr anharmonic ladder. As the squeezing amplitude—and therefore $|\alpha|^2$ —grows, the spectrum becomes pairwise degenerate with levels of different photon-number parity approaching each other in an exponential fashion. We refer to this exponential approach of energy levels as spectral kissing. This is

the first observation of a controllable highly excited (quasi)energy spectrum of a *driven* system.

To understand the observed spectrum, we now explore a semiclassical model. The limiting classical orbit, which is the separatrix of the wells in Fig. 1(b), forms a figure-8 curve known as Bernoulli’s lemniscate [70]. In an approximation along the lines of Bohr’s action quantization, its area in units of Planck’s constant h counts the number N of quantum states in the wells. Analytically, we find $N = \epsilon_2/\pi K = |\alpha|^2/\pi$. Every time N coincides with an integer value, a new pair of excited semiclassical orbits is captured by the wells (see Appendix G). The vertical dashed lines in Figs. 3(a), 3(c), and 3(d) correspond to this semiclassical condition. As the squeezing amplitude ϵ_2 increases, the captured levels sink under the metapotential barrier and, coupled only by quantum tunneling, exponential level kissing takes place.

The most remarkable consequence of the pairwise level kissing is the staircase-shaped increase of the lifetime T_X as a function of the squeezing amplitude, which was independently found theoretically [92,93]. This we show in Fig. 3(d). This stepwise increase can be understood, to a

first approximation, using Bohr's action quantization. For $\epsilon_2 \ll K$, T_X corresponds to loss of coherence of the superposition between the ground state and the first excited state of a Kerr oscillator (T_{2R}), but increases exponentially as each of the two metapotential wells becomes wide enough to host one action quantum each ($\epsilon_2/\pi K \sim 1$, first vertical dashed line). The exponential increase stops when excitations to the first pair of excited states (\hat{a}^\dagger -like events) become the limiting factor. An excitation into these states will allow the transition between wells. The incoherent environment-induced activation time thus plateaus at $\sim 250 \mu\text{s}$ until Bohr's quantization condition is met again and the first pair of excited states is captured by the metapotential wells ($\epsilon_2/\pi K \sim 2$, second vertical dashed line). At this point, the tunnel splitting between the first pair of excited states vanishes and the increase of lifetime resumes. This cycle repeats itself for the next pair of excited states as shown by the third rising slope in lifetime at $\epsilon_2/\pi K \sim 3$ (third vertical dashed line). We thus interpret the experimental data as a manifestation of action quantization modifying the incoherent environment-induced activation time T_X across the double-well barrier [27,43].

Despite the success of action quantization to explain features of our experimental data, the argument is semiclassical and unitary. It thus neglects tunneling and dissipation, but it can be refined. We now refine our modeling with a simple RWA Lindbladian model given by the master equation,

$$\dot{\rho} = \frac{1}{i\hbar} [\hat{H}_{\text{SK}} - \hbar\Delta\hat{a}^\dagger\hat{a}, \rho] + \kappa_1(1+n_{\text{th}})\mathcal{D}[\hat{a}]\rho + \kappa_1 n_{\text{th}}\mathcal{D}[\hat{a}^\dagger]\rho, \quad (3)$$

where $\mathcal{D}[\hat{O}]$ is the standard Lindbladian dissipator of jump operator \hat{O} defined by $\mathcal{D}[\hat{O}]\bullet := \hat{O}\bullet\hat{O}^\dagger - (\hat{O}^\dagger\hat{O}\bullet + \bullet\hat{O}^\dagger\hat{O})/2$, and which contains the Hamiltonian dynamics governed by Eq. (2) with an added detuning $\Delta = \omega_a - \omega_d/2$ term, as well as Markovian single-photon gain and loss at the measured coupling rate κ_1 and with a phenomenological temperature given by a mean photon number in the bath n_{th} . We also include low-frequency detuning noise by sampling Δ from a normal distribution with mean 0 and width ~ 10 kHz to account for flux noise and reproduce the behavior of our experimental data for $\epsilon_2/K = |\alpha|^2 \lesssim 2$. We observe that the incoherent activation time T_X in the regime $|\alpha|^2 \lesssim 2$ increases rapidly; a sufficiently high barrier makes the ground-state Kerr-cat qubit insensitive to frequency fluctuations in the resonance of the circuit. Such dephasing ceases to be the limiting mechanism when the coherent states become nonoverlapping, a condition captured by Bohr's quantization (see Appendix F and Ref. [75]). Once low-frequency detuning errors become irrelevant, the first plateau in Fig. 3(d) is reached.

For values of $|\alpha|^2$ between π and 2π , the lifetime of the states remains essentially constant, limited by thermal

excitation toward the first pair of excited states that have energies close to the metapotential barrier. The model including only single-photon gain and loss predicts a simple expression for the lifetime saturation value that reads $T_X = (n_{\text{th}}\kappa_1)^{-1}$. The predictions of this Lindbladian model are shown in the colored curves in Fig. 3(d).

The model correctly predicts that the rising edge after the first plateau occurs at the value of $|\alpha|^2$ where the dissipation rate κ_1 overcomes the nonlinear tunnel splitting between the first pair of excited states δ_1 (see Appendix and Refs. [92,93]): A thermal excitation populating the first pair of nondegenerate excited states induces tunneling from one well to the other at rate δ_1 , while single-photon dissipation fights against this effect by bringing the population back to the ground state at rate κ_1 . Thus, if $\delta_1 < \kappa_1$, the tunneling between wells via the first pair of excited states is reduced by dissipation. This explains in semiquantitative terms why the elementary picture based on action quantization works well for our experiment: The nonlinear splitting of the n th pair of excited levels δ_n vanishes as the eigenstates are captured by the lemniscate [94]. At that point, the splitting is exponentially reduced by the tunnel effect and fulfills the condition $\delta_n < \kappa_1$ almost immediately thereafter [95]. The slight downward slope within each plateau in the data can be explained by adding higher-order dissipators to the model (see Fig. 11 in Appendix G).

Our experiment illustrates how the classical law of thermal activation across a barrier, known as the Arrhenius's law, is modified by Bohr's action quantization. The activation across a barrier has a long history [25,27–30,43] (for spin analogs, see Refs. [46,47,96]). In the "classical limit" $\epsilon_2/K \gg 1$ (formally equivalent here to $\hbar \rightarrow 0$), the expected smooth exponential behavior is recovered in the model. Alternatively, if $\kappa_1 \gtrsim K$, the classical behavior expected from Arrhenius's law is recovered even for moderate values of ϵ_2/K too (see Fig. 14 in Appendix G).

While we have explained the presence and location of the plateaus in the measurements of T_X , there is no quantitative agreement between the simple RWA Lindbladian model and the data. The data traverse isotherms in Fig. 3(d) and seem to suggest that the simple model requires the introduction of extra heating terms. Trivial heating of the attenuators in the microwave lines is improbable, as checked by changing the duty cycle of the measurement sequence. We remark that, in our experiment and regardless of this discrepancy, the phase flips ($|+\alpha\rangle \leftrightarrow |-\alpha\rangle$) of our Kerr-cat qubit as measured here by T_X are robust to gate drives, readout drives, and flux noise as expected (see Fig. 7 in Appendix E, Fig. 6 in Appendix D, and Fig. 11 in Appendix G, respectively). Further work, probably requiring beyond-RWA dissipators [65,68,97–99], will be needed to improve the present state of the modeling (see Ref. [65]).

We also measure the lifetime T_{YZ} of the Schrödinger cat superpositions of $|\pm\alpha\rangle$, which are all degenerate

ground states of Eq. (2) for $|\alpha| > 0$. The results are shown in Fig. 3(e). As expected, the lifetime T_{YZ} does not present steps and is well described by standard dissipators. This is because the decoherence of cat states is dominated by single-photon-loss events while the system remains in the ground states. The experimental sequence used for this measurement is shown in Fig. 3(f). The interruption of the stabilization drive for a period of $784 \text{ ns} \approx \pi/2K$ maps parityless cat states into coherent states (and vice versa) under free Kerr evolution for preparation and measurement (see Fig. 10 in Appendix G and [48]). The lifetime T_{YZ} is measured as the decay time of oscillation between cat states. This is achieved by applying a drive at $\omega_d/2$ while the squeezing drive is on. Under these conditions, the coherent states remain locked to the minima of the wells while the phase-space interference fringes of the cat states roll, continuously changing the cat parity from odd to even and producing an oscillatory behavior in the data (see Appendices E and G and [48,62]). The black line in Fig. 3(e) corresponds to a prediction with no adjustable parameters given by $T_1/2\langle\bar{n}\rangle$, where $\langle\bar{n}\rangle = |\alpha|^2(1 + e^{-4|\alpha|^2})/(1 - e^{-4|\alpha|^2})$ is the time-averaged number of photons in the oscillation (see Appendix G). The gray band accounts for the uncertainty in the independently determined T_1 .

Note that the full Hamiltonian control we have over the system provides different operating points. If highest average cat-qubit coherence is desired, we choose $\epsilon_2/K = 1.85$ for which we measure, as described in Figs. 4(a) and 4(b), lifetimes of $T_X \gtrsim 97 \mu\text{s}$ [results shown in Fig. 4(c)] and $T_{YZ} \gtrsim 5.7 \mu\text{s}$ [Fig. 4(d)]. Alternatively, it is possible to increase T_X at the expense of some reduction of T_{YZ} . With this in mind, we note that in addition to the drive amplitude, we can tune the drive frequency to exploit the rich nonlinear dynamics of our double-well system. By pumping the parametric squeezing off-resonantly, a quadratic static effective term arises in Eq. (2): $-\Delta\hat{a}^\dagger\hat{a}$, where $\Delta = \omega_d/2 - \omega_a$ is the drive detuning. Applying Bohr quantization to the separatrix in the new metapotential surface, we find that the number of bound semiclassical orbits now reads $N = (\epsilon_2/\pi K) - (\Delta/8K)$. We then reduce the squeezing amplitude, and thus the associated anomalous heating, to $\epsilon_2/K = 8.9$ and set $\Delta/2\pi = -4.5 \text{ MHz} = 14K/2\pi$. In this condition, we measure a lifetime of $T_X = (1.102 \pm 0.008) \text{ ms}$ —an increase of $T_X/T_2^* \sim 440$ times—while maintaining coherent control over the cat states for a time $T_{YZ} = (0.76 \pm 0.08) \mu\text{s}$. We show these results in Figs. 4(e) and 4(f). Note, nonetheless, that interference effects between quantum phase-space trajectories take place as a function of Δ [100,101] and contribute also to the lifetime enhancement. A detailed experimental exploration of lifetime control with the detuning parameter Δ is communicated elsewhere [102]; see also recent theory work exploiting the detuning parameter [103,104].

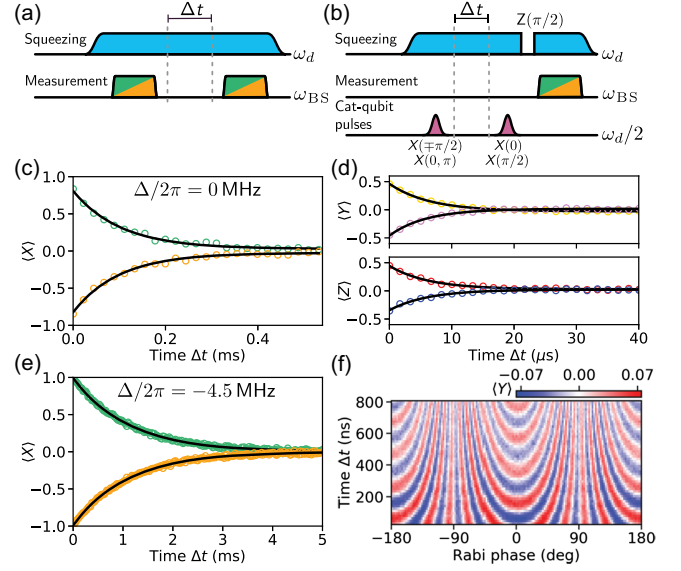


FIG. 4. Global error protection and large error bias cat qubits. (a) Pulse sequence for measurement of T_X coherent state lifetime in (c) and (e). (b) Pulse sequence for measurement of T_{YZ} cat-state lifetimes in (d). (c),(d) Kerr-cat qubit operating at $\Delta = 0$ and $\epsilon_2/K = 1.85$ where average coherence surpasses that of the bare system. (c) Green and orange data for preparation in $|\pm\alpha\rangle$ and black lines are single-exponential fits with decay time $T_{+X} = (101 \pm 4) \mu\text{s}$ and $T_{-X} = (103 \pm 4) \mu\text{s}$. (d) Cat-state coherences for the two parityless cats (top, yellow and pink) and for the even and odd parity cats (bottom, red and blue). Black lines are single-exponential fits with $T_{+Y} = (5.9 \pm 0.2) \mu\text{s}$, $T_{-Y} = (6.5 \pm 0.2) \mu\text{s}$, and $T_{+Z} = (6.1 \pm 0.1) \mu\text{s}$, $T_{-Z} = (6.2 \pm 0.4) \mu\text{s}$, respectively. (e),(f) Operation point with drive detuning $\Delta/2\pi = -4.5 \text{ MHz}$ and $\epsilon_2/K = 8.9$ implying a mean photon number of 15. (e) Lifetime measurement for $|\pm\alpha\rangle$ (green and orange). The black line is an exponential fit with timescale $T_{\pm X} = (1.102 \pm 0.008) \text{ ms}$. (f) Oscillations between cat states as a function of single-photon drive time and phase [pulse sequence as in Fig. 3(f)]. Fits of the line cut at zero phase yield a coherent oscillation with decay time of $T_{YZ} = (0.76 \pm 0.08) \mu\text{s}$.

IV. REMARKS AND CONCLUSION

We have experimentally realized a squeeze-driven Kerr oscillator by applying a strong microwave drive to a SNAIL transmon and resolved excited quantum levels. The double-well spectroscopic fingerprint of pairwise kissing is in excellent agreement with a static effective theory of our quantum driven system with no adjustable parameters. Finally, we observe the remarkable signature of action quantization in the incoherent environment-induced activation time T_X across the double-well barrier.

Our results indicate that, depending on the requirements of a desired quantum information application, different experimental operating points can be selected. For quantum information applications, for example, the operating point shown in Figs. 4(c) and 4(d) ($\Delta = 0$ and $\epsilon_2/K = 1.85$), the average decoherence rate over the six cardinal states of the Kerr-cat qubit Bloch sphere is smaller than that of the qubit

encoded in the two lowest lying Fock states in our system by an autonomous error protection gain factor of 2.8 (see Appendix B 1). We remark, though, that the Kerr-cat qubit, like a repetition code [105,106], is designed to correct logical errors along only one axis of the Bloch sphere.

If qubit applications instead require a “large error bias” ($T_X \gg T_{YZ} > 0$) [49,51–53], one could choose to operate the Kerr-cat qubit at $\epsilon_2/K = 10$, where we measure $T_X = 500 \mu\text{s}$ ($T_X/T_2^* \sim 200$) and $T_{YZ} = 1 \mu\text{s}$. Note that for quantum applications, large error bias demands that the short timescale, here T_{YZ} , remains long enough to perform the required coherent operations and high-fidelity measurements.

With detuning, T_X is increased by an additional factor of 2 preserving finite cat lifetime and thus a large bias ($T_X/T_{YZ} \sim 1450$, at $\Delta = 14K$, and $\epsilon_2/K = 8.9$). This result demands the extension of the theoretical and experimental techniques to treat Hamiltonian stabilization of bosonic qubits, now for off resonant with respect to 2 times the SNAIL small oscillation frequency driving.

Short-term applications of our system include the realization of a pair of strongly driven Kerr oscillators operated simultaneously and in interaction (see Fig. 1). This Kerr-cat molecule will be of great interest for the implementation of single and multiqubit gates in a quantum processor with reduced hardware overhead [50–54]. Another immediate use of our system is as a fault-tolerant ancilla [49] for other bosonic error correction codes [107,108]. The large error bias and the possibility to perform fast Raman gates via the excited-state spectrum are enabling assets of our implementation [109–111], leading to the development of a wealth of now possible techniques.

In the longer term, the setup presented in this work can be used to perform new experiments of fundamental interest. Among them we mention the demonstration of new dynamical Casimir effects and quantum heating [112,113], dynamical tunneling and interference in the classically forbidden region [100], quantum simulation of excited-state phase transitions in nuclear and molecular systems [114–116], fluids of light [117], quantum annealing and quantum simulation of Ising models [73,86,118,119], and the exploration of quantum chaos in systems with a direct classical correspondence [67,120–122].

ACKNOWLEDGMENTS

We acknowledge the contributions of L. Frunzio, A. Grimm, V. V. Sivak, and I. Gracia-Mata, and discussions with J-M. Raimond, V. Shumeiko, M. Dykman, H. Goto, H. Putterman, K. Noh, C. Regal, V. Kurilovich, P. Kurilovich, L. Santos, and F. Perez-Bernal. Facilities use was supported by YINQE and the Yale SEAS cleanroom. We also acknowledge the support of the Yale Quantum Institute. This research was sponsored by the Army Research Office (ARO) and was accomplished under Grants No. W911NF-18-1-0212, No. W911NF-16-1-0349, and No. W911NF-23-1-0051 by

the Air Force Office of Scientific Research (AFOSR) under Award No. FA9550-19-1-0399, and by the National Science Foundation (NSF) under Grant No. 1941583 and Centers for Chemical Innovation (CCI) Grant No. 2124511.

N. E. F. designed and fabricated the superconducting device and package with input from C. L., B. J. C., S. P., and M. H. D. N. E. F. and R. G. C. designed and performed the experiments, built the setup, and took and analyzed the data under the supervision of M. H. D. B. J. C. and V. R. J. fabricated the quantum-limited amplifier used for readout. J. V. and X. X. proposed and insisted on the importance of off-resonant pumping and proposed the dynamical Bohr quantization to our system. Q. S. and R. G. C. developed numerical tools to analyze decoherence with support from N. E. F., S. P., S. M. G., and M. H. D. R. G. C., N. E. F., J. V., and M. H. D. wrote the manuscript with input from all authors.

R. J. S. is a founder and equity holder, and S. P. and S. M. G. receive consulting fees and/or hold equity in Quantum Circuits, Inc. M. H. D. has presently an advisory role at Google Quantum AI. N. E. F. is presently employed by Nord Quantique. The views and conclusions contained in this document belong to the authors and should not be interpreted as representing the official policies, either expressed or implied, of the grant agencies, or the U.S. Government. The U.S. Government is authorized to reproduce and distribute reprints for Government purposes notwithstanding any copyright notation herein.

APPENDIX A: DERIVATION OF THE STATIC-EFFECTIVE SQUEEZED KERR HAMILTONIAN

The SNAIL-transmon Josephson circuit [57] is well modeled as a nonlinear oscillator. To compute the static-effective squeezed Kerr oscillator Hamiltonian, we consider the Hamiltonian of a driven nonlinear oscillator in the bosonic basis,

$$\frac{\hat{H}(t)}{\hbar} = \omega_o \hat{a}^\dagger \hat{a} + \sum_{m \geq 3} \frac{g_m}{m} (\hat{a} + \hat{a}^\dagger + \Pi e^{-i\omega_o t} + \Pi^* e^{i\omega_o t})^m, \quad (\text{A1})$$

where the oscillator is characterized by ω_o , its bare frequency, g_m/m , its m th-order nonlinearity, and \hat{a}^\dagger the bosonic creation operator satisfying the standard commutation relation between bosonic operators: $[\hat{a}, \hat{a}^\dagger] = 1$. The Hamiltonian in Eq. (1) is related to Eq. (A1) by a displacement transformation into the linear response of the oscillator, where the effective amplitude of the displacement is $\Pi = (2\Omega_d/3\omega_o)$.

Next, we seek a transformed frame in which the nonlinear Hamiltonian rates are small compared to the drive

subharmonic frequency $\omega_d/2 \approx \omega_o$. We achieve this by going into a rotating frame induced by $(\omega_d/2)\hat{a}^\dagger \hat{a}$, transforming Eq. (A1) to

$$\frac{\hat{H}(t)}{\hbar} = -\delta \hat{a}^\dagger \hat{a} + \sum_{m \geq 3} \frac{g_m}{m} (\hat{a} e^{-i\omega_d t/2} + \quad (A2)$$

$$\hat{a}^\dagger e^{i\omega_d t/2} + \Pi e^{-i\omega_d t} + \Pi^* e^{i\omega_d t})^m, \quad (A3)$$

where $\delta = (\omega_d/2) - \omega_o \ll \omega_d$.

From Eq. (A2), we compute, perturbatively, an effective Hamiltonian that captures the relevant dynamics in this displaced rotating frame. Here, we introduce $\varphi_{\text{ZPS}} \ll 1$, the zero-point spread of the phase across the Josephson junction which is the perturbative parameter of our expansion. The source of the nonlinearity being the Josephson potential guarantees a hierarchy in the Hamiltonian nonlinearities. The m th nonlinearity is order $m-2$ in the perturbation, i.e., $g_m/m = \mathcal{O}(\omega_o \varphi_{\text{ZPS}}^{m-2})$ for $m \geq 3$, where φ_{ZPS} is the zero-point spread of the superconducting phase across the nonlinear element. With the placement of our drive, we ensure that $\delta \lesssim g_3$.

Following Ref. [65], we find an effective Hamiltonian with following structure:

$$\hat{H}_{\text{eff}} = \sum_{n \geq 1} \hat{H}_{\text{eff}}^{(n)}, \quad \hat{H}_{\text{eff}}^{(n)} = \sum_{k \geq 0} \hat{H}_{\text{eff}[k]}^{(n)} |\Pi|^{2k}, \quad (A4)$$

where the superscript n denotes the order in the perturbation parameter and the subscript k denotes the number of participating drive excitation pairs.

At orders 1 and 2, we find the effective Hamiltonian takes the form

$$\frac{\hat{H}_{\text{eff}}}{\hbar} = -\Delta \hat{a}^\dagger \hat{a} - K \hat{a}^{\dagger 2} \hat{a}^2 + \epsilon_2 \hat{a}^{\dagger 2} + \epsilon_2^* \hat{a}^2 + \mathcal{O}(\omega_o \varphi_{\text{ZPS}}^3), \quad (A5)$$

with

$$\Delta = \sum_{n=1,2} \Delta^{(n)}, \quad K = \sum_{n=1,2} K^{(n)}, \quad \epsilon_2 = \sum_{n=1,2} \epsilon_2^{(n)}, \quad (A6)$$

where we find

$$\begin{aligned} -\Delta^{(1)} &= -\delta, & -\Delta^{(2)} &= -\sum_{k=0,1} \Delta_{[k]}^{(2)} |\Pi|^{2k}, \\ -\Delta_{[0]}^{(2)} &= 3g_4 - \frac{20}{3} \frac{g_3^2}{\omega_o}, & -\Delta_{[1]}^{(2)} &= 6g_4 - 9 \frac{g_3^2}{\omega_o}, \\ -K^{(1)} &= 0, & -K^{(2)} &= \frac{3g_4}{2} - \frac{10}{3} \frac{g_3^2}{\omega_o}, \\ \epsilon_2^{(1)} &= g_3 \Pi, & \epsilon_2^{(2)} &= 0. \end{aligned} \quad (A7)$$

We remark that $\Delta_{[0]}^{(2)}$ and $\Delta_{[1]}^{(2)}$ are the well-known Lamb shift and ac Stark shift, respectively. Similarly, the dependence of $K^{(2)}$ and $\epsilon_2^{(1)}$ on external flux have been previously verified in SNAIL parametric amplifiers [58,59].

At order 3, following the notation introduced above, we find the effective Hamiltonian as

$$\frac{\hat{H}_{\text{eff}}^{(3)}}{\hbar} = -\Delta^{(3)} \hat{a}^\dagger \hat{a} - K^{(3)} \hat{a}^{\dagger 2} \hat{a}^2 + \quad (A8)$$

$$\epsilon_2^{(3)} \hat{a}^{\dagger 2} + \epsilon_2^{(3)*} \hat{a}^2 + \epsilon_2^{\prime(3)} \hat{a}^{\dagger 3} \hat{a} + \epsilon_2^{\prime*(3)} \hat{a}^\dagger \hat{a}^3, \quad (A9)$$

where

$$-\Delta^{(3)} = -\frac{20\delta g_3^2}{3\omega_o^2} - \frac{17\delta g_3^2}{2\omega_o^2} |\Pi|^2, \quad -K^{(3)} = -\frac{10\delta g_3^2}{3\omega_o^2}, \quad (A10)$$

$$\epsilon_2^{(3)} = \left(6g_5 - \frac{141}{10} \frac{g_3 g_4}{\omega_o} + \frac{221}{180} \frac{g_3^3}{\omega_o^2} \right) |\Pi|^2 \Pi \quad (A11)$$

$$+ \left(6g_5 - \frac{63}{4} \frac{g_3 g_4}{\omega_o} + \frac{1}{3} \frac{g_3^3}{\omega_o^2} \right) \Pi, \quad (A12)$$

$$\epsilon_2^{\prime(3)} = \left(4g_5 - \frac{21}{2} \frac{g_3 g_4}{\omega_o} + \frac{2}{9} \frac{g_3^3}{\omega_o^2} \right) \Pi. \quad (A13)$$

Note that the Hamiltonian terms $\propto \hat{a}^{\dagger 3} \hat{a} + \hat{a}^\dagger \hat{a}^3 = \hat{a}^{\dagger 2} (\hat{a}^\dagger \hat{a}) + (\hat{a}^\dagger \hat{a}) \hat{a}^2$ represent a photon-number-dependent squeezing interaction.

With this understanding, we remark that even at the third order the effective Hamiltonian contains no parasitic terms, a quantum manifestation of the robustness of the period-doubling bifurcation.

At order 4, we find a four-photon drive, and the first nonsqueezing drive term, in the effective Hamiltonian:

$$\frac{\hat{H}_{\text{eff}}^{(4)}}{\hbar} = -\Delta^{(4)} \hat{a}^\dagger \hat{a} - K^{(4)} \hat{a}^{\dagger 2} \hat{a}^2 - \lambda^{(4)} \hat{a}^{\dagger 3} \hat{a}^3 \quad (A14)$$

$$+ \epsilon_4^{(4)} \hat{a}^{\dagger 4} + \epsilon_4^{(4)*} \hat{a}^4 + \hat{a}^{\dagger 2} \left(\epsilon_{2,\Pi}^{(4)} + \epsilon_{2,\hat{n}}^{(4)} \hat{a}^\dagger \hat{a} \right) \quad (A15)$$

$$+ \left(\epsilon_{2,\Pi}^{*(4)} + \epsilon_{2,\hat{n}}^{*(4)} \hat{a}^\dagger \hat{a} \right) \hat{a}^2, \quad (A16)$$

where

$$\Delta^{(4)} = \sum_{k=0,1,2} \Delta_{[k]}^{(4)} |\Pi|^{2k},$$

$$\text{and } K^{(4)} = \sum_{k=0,1} K_{[k]}^{(4)} |\Pi|^{2k}.$$

The expressions for all the coefficients of Eq. (A14) are displayed below:

$$\begin{aligned}
-\Delta_{[0]}^{(4)} &= 15g_6 - \frac{220}{3} \frac{g_3 g_5}{\omega_o} - 18 \frac{g_4^2}{\omega_o} + 188 \frac{g_3^2 g_4}{\omega_o^2} - \frac{20}{3} \frac{\delta^2 g_3^2}{\omega_o^4}, \\
-\Delta_{[1]}^{(4)} &= \left(60g_6 - 232 \frac{g_3 g_5}{\omega_o} - \frac{108}{5} \frac{g_4^2}{\omega_o} \right. \\
&\quad \left. + \frac{1342}{5} \frac{g_3^2 g_4}{\omega_o^2} + \frac{1612}{45} \frac{g_3^4}{\omega_o^3} - \frac{33}{4} \frac{\delta^2 g_3^2}{\omega_o^3} \right), \\
-\Delta_{[2]}^{(4)} &= \left(30g_6 - \frac{644}{5} \frac{g_3 g_5}{\omega_o} + 9 \frac{g_4^2}{\omega_o} \right. \\
&\quad \left. + \frac{15113}{150} \frac{g_3^2 g_4}{\omega_o^2} + \frac{257963}{2700} \frac{g_3^4}{\omega_o^3} \right), \\
-K_{[0]}^{(4)} &= \left(15g_6 - 84 \frac{g_3 g_5}{\omega_o} - \frac{153}{8} \frac{g_4^2}{\omega_o} \right. \\
&\quad \left. + 225 \frac{g_3^2 g_4}{\omega_o^2} - \frac{10}{3} \frac{\delta^2 g_3^2}{\omega_o^4} - \frac{470}{3} \frac{g_3^4}{\omega_o^3} \right), \\
-K_{[1]}^{(4)} &= \left(30g_6 - 116 \frac{g_3 g_5}{\omega_o} - \frac{54}{5} \frac{g_4^2}{\omega_o} + \frac{671}{5} \frac{g_3^2 g_4}{\omega_o^2} + \frac{806}{45} \frac{g_3^4}{\omega_o^3} \right), \\
-\lambda^{(4)} &= \frac{10}{3} g_6 - \frac{56}{3} \frac{g_3 g_5}{\omega_o} - \frac{17}{4} \frac{g_4^2}{\omega_o} + 50 \frac{g_3^2 g_4}{\omega_o^2} - \frac{940}{27} \frac{g_3^4}{\omega_o^3}, \\
\epsilon_4^{(4)} &= \left(\frac{5}{2} g_6 + \frac{2}{15} \frac{g_3 g_5}{\omega_o} - \frac{33}{4} \frac{g_4^2}{\omega_o} - \frac{101}{24} \frac{g_3^2 g_4}{\omega_o^2} + \frac{221}{18} \frac{g_3^4}{\omega_o^3} \right) \Pi^2, \\
\epsilon_{2,\hat{n}}^{(4)} &= \left(\frac{353 - \delta g_3 g_4}{24} \frac{1}{\omega_o^2} + \frac{521 - \delta g_3^3}{54} \frac{1}{\omega_o^3} \right) \Pi, \\
\epsilon_{2,\Pi}^{(4)} &= \left(\frac{10669 - \delta g_3 g_4}{600} \frac{1}{\omega_o^2} + \frac{46313 - \delta g_3^3}{5400} \frac{1}{\omega_o^3} \right) |\Pi|^2 \Pi \\
&\quad + \left(\frac{353 - \delta g_3 g_4}{16} \frac{1}{\omega_o^2} + \frac{521 - \delta g_3^3}{36} \frac{1}{\omega_o^3} \right) \Pi.
\end{aligned}$$

All in all, the squeezed Kerr Hamiltonian is not modified structurally by contributions beyond the rotating wave approximation, up to the fourth order. This theoretical understanding explains our clean experimental realization of the squeezed Kerr Hamiltonian with a driven SNAIL.

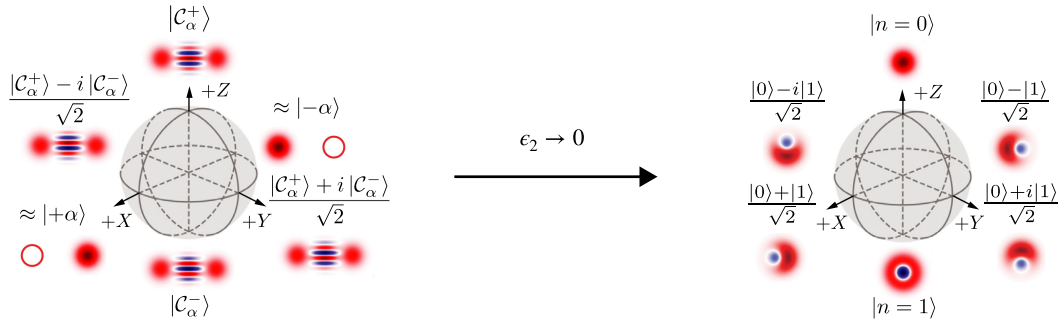


FIG. 5. The adiabatic mapping of the Kerr-cat qubit Bloch sphere to the Fock encoding. The logical states in the Kerr-cat qubit and their parity conserving adiabatic mapping to the two-level transmon Bloch sphere.

APPENDIX B: BLOCH SPHERE FOR THE KERR-CAT QUBIT

The ground states of Hamiltonian Eq. (2) in the main text are exactly degenerate Schrödinger cat states $|C_\alpha^\pm\rangle$. Restricting our system to these two ground states we define a computational Kerr-cat qubit subspace. Its Bloch sphere is shown in Fig. 5. The even and odd Schrödinger cat states are taken to be in the north and south poles of the sphere since they adiabatically map to the zero and one Fock states of the transmon Kerr oscillator as $\epsilon_2 \rightarrow 0$. This provides a physically realizable mapping [48] to standard Bloch sphere used in the superconducting circuit platform.

Under this convention we define the basis for the computational space by

$$\begin{aligned}
|\pm Z\rangle &= |C_\alpha^\pm\rangle \\
&= \mathcal{N}_\alpha^\pm (|+\alpha\rangle \pm |-\alpha\rangle) \\
&= \mathcal{N}_\alpha^\pm e^{-|\alpha|^2/2} \sum_{n=0}^{\infty} (1 \pm (-1)^n) \frac{\alpha^n}{\sqrt{n!}} |n\rangle, \\
\mathcal{N}_\alpha^\pm &= 1/\sqrt{2(1 \pm e^{-2|\alpha|^2})}, \tag{B1}
\end{aligned}$$

where \mathcal{N}_α^\pm are normalization constants.

The mean photon number in these states is given by $\bar{n}_\pm = \langle C_\alpha^\pm | \hat{a}^\dagger \hat{a} | C_\alpha^\pm \rangle = r^{\pm 2} |\alpha|^2$, and

$$r = \frac{\mathcal{N}_\alpha^+}{\mathcal{N}_\alpha^-} = \frac{\sqrt{1 - e^{-2|\alpha|^2}}}{\sqrt{1 + e^{-2|\alpha|^2}}} \rightarrow 1 - e^{-2|\alpha|^2}, \tag{B2}$$

where the arrow corresponds to the expressions in the limit $\epsilon_2 \gg K$ ($|\alpha|^2 \gg 1$). We thus define the other two complementary and mutually nonbiased Pauli basis as

$$\begin{aligned}
|\pm X\rangle &= \frac{1}{\sqrt{2}} (|C_\alpha^+\rangle \pm |C_\alpha^-\rangle) \rightarrow |\pm \alpha\rangle, \\
|\pm Y\rangle &= \frac{1}{\sqrt{2}} (|C_\alpha^+\rangle \pm i|C_\alpha^-\rangle) \rightarrow \frac{1}{\sqrt{2}} (|+\alpha\rangle \mp i|-\alpha\rangle). \tag{B3}
\end{aligned}$$

TABLE I. Projection of some “local” (low order in \hat{a} and \hat{a}^\dagger) phase-space operators over the oscillator to the Kerr-cat logical manifold. They represent the main source of errors in bosonic codes. Besides the exact expression for all values of α , we provide instructive limits for large and small photon number. Note that in the large cat limit the operators contain corrections of at most $\mathcal{O}(\alpha^2 e^{-4|\alpha|^2})$.

	$\alpha \rightarrow 0$	α	Large $ \alpha $
\hat{a}	$\frac{1}{2}(\hat{X} + i\hat{Y})$	$\alpha \frac{(r+r^{-1})}{2}\hat{X} - i\alpha \frac{(r-r^{-1})}{2}\hat{Y}$	$\alpha\hat{X} + i\alpha e^{-2 \alpha ^2}\hat{Y}$
\hat{a}^\dagger	$\frac{1}{2}(\hat{X} - i\hat{Y})$	$\alpha^* \frac{(r+r^{-1})}{2}\hat{X} + i\alpha^* \frac{(r-r^{-1})}{2}\hat{Y}$	$\alpha^*\hat{X} - i\alpha^* e^{-2 \alpha ^2}\hat{Y}$
$\hat{a}^\dagger \hat{a}$	$\frac{1}{2}(\hat{I} - \hat{Z})$	$ \alpha ^2 \frac{(r^2+r^{-2})}{2}\hat{I} + \alpha ^2 \frac{(r^2-r^{-2})}{2}\hat{Z}$	$ \alpha ^2\hat{I} - 2 \alpha ^2 e^{-2 \alpha ^2}\hat{Z}$

The Pauli operators are then defined as

$$\begin{aligned}\hat{X} &= |\mathcal{C}_\alpha^+\rangle\langle\mathcal{C}_\alpha^-| + |\mathcal{C}_\alpha^-\rangle\langle\mathcal{C}_\alpha^+|, \\ \hat{Y} &= -i|\mathcal{C}_\alpha^+\rangle\langle\mathcal{C}_\alpha^-| + i|\mathcal{C}_\alpha^-\rangle\langle\mathcal{C}_\alpha^+|, \\ \hat{Z} &= |\mathcal{C}_\alpha^+\rangle\langle\mathcal{C}_\alpha^+| - |\mathcal{C}_\alpha^-\rangle\langle\mathcal{C}_\alpha^-|,\end{aligned}\quad (\text{B4})$$

and their scaling with α is shown in Table I.

1. Definition of autonomous error correction gain

Given that we have defined the Bloch sphere, we may also define the average coherence of the Bloch sphere as

$$\gamma = \frac{1}{6} \sum_{i=\pm X, \pm Y, \pm Z} \frac{1}{T_i}, \quad (\text{B5})$$

where T_i is the decay time constant for preparing the system in one of the six cardinal states ($|i\rangle$) of the Bloch sphere.

For the Fock qubit, we use the measured Ramsey decay to calculate $(1/T_{+X} + 1/T_{-X} + 1/T_{+Y} + 1/T_{-Y})/4 = 1/T_{2R}$, and the measured single excitation decay time to calculate $1/T_{+Z} + 1/T_{-Z} = 1/T_1$; this defines the average coherence of the Fock qubit.

For the Kerr-cat qubit, we either independently measure each cardinal state’s coherence or use T_{YZ} as in Fig. 3(e) to summarize the coherence on the YZ plane. The combination of these measurements allows us to define the autonomous quantum error correction gain factor $\gamma_{\text{Fock}}/\gamma_{\text{cat}}$, which efficiently summarizes the Kerr-cat qubit’s performance as a quantum memory relative to the bare Fock qubit encoding. At the bias point shown in Figs. 4(c) and 4(d), this leads to an autonomous quantum error correction gain factor of 2.8 beyond breakeven.

2. Photon loss

It is interesting to notice that in a realistic scenario, the presence of dissipation will slightly deform the computational states. We analyze this by considering only single- and two-photon loss. We generalize the Hamiltonian in Eq. (2) by casting the no-jump Hamiltonian of the open quantum system as

$$\hat{H}_{\text{SK}}^{\text{no-j}}/\hbar = -\tilde{\Delta}\hat{a}^\dagger\hat{a} - \tilde{K}\hat{a}^{\dagger 2}\hat{a}^2 + \epsilon_2(\hat{a}^{\dagger 2} + \hat{a}^2). \quad (\text{B6})$$

Here the Hamiltonian constants are complex numbers: Generalized detuning $\tilde{\Delta} = \Delta + i\kappa_1/2$, and generalized Kerr $\tilde{K} = K + i\kappa_2/2$, where κ_1 and κ_2 are the single- and two-photon-loss rates in the system. The phase-space center of mass of the new eigenstates is obtained by displacing this no-jump Hamiltonian by a complex amplitude $\tilde{\alpha} = |\tilde{\alpha}|e^{-i(\arg \epsilon_2/\tilde{K})/2}e^{i\tilde{\phi}}$ and solving for null-linear terms in the displaced Hamiltonian. The dissipative eigenstates are found to be centered at

$$|\tilde{\alpha}|^2 = \frac{1}{2|\tilde{K}|^2} \left(-\Delta K + \frac{\kappa_1\kappa_2}{4} \right) \quad (\text{B7})$$

$$\pm \sqrt{\left| \frac{\epsilon_2}{\tilde{K}} \right|^2 - \left(\frac{K\kappa_1 - \Delta\kappa_2}{4|\tilde{K}|^2} \right)^2}, \quad (\text{B8})$$

$$\sin(2\tilde{\phi}) = \frac{K\kappa_1 - \Delta\kappa_2}{4|\epsilon_2||\tilde{K}|}, \quad (\text{B9})$$

where the + solution is valid when $|\epsilon_2|^2 \geq (\Delta^2 + \kappa_1^2/4)/4$, which is beyond the parametric instability exploited for parametric amplification and inside the double-well regime of bifurcation relevant to this work (see Ref. [88] for in-depth discussion). Note that the cat size also increases with $-\Delta$, and thus increases the protection of the coherent states to perturbations.

Examining the equation for $\tilde{\phi}$, the remarkable π periodicity of the solutions is evident. This is the quantum manifestation of a classically robust period-doubling bifurcation and it contains the essence of the noise-resilient properties of the our cat qubit. The solutions are always maximally spaced in phase space forming an angle of 180° . For $\Delta = 0$ and in the bifurcation regime, we have that the ground-state manifold is spanned by the coherent states $|\pm \tilde{\alpha}\rangle$ even in the presence of dissipation.

APPENDIX C: SUPERCONDUCTING PACKAGE AND DESIGN CHOICES

In this appendix, we outline the key design principles for the superconducting package and circuit quantum

electrodynamics (cQED) system. The overarching design goal was to incorporate two capacitively coupled SNAIL-transmon circuits that could each be individually stabilized with a squeezing drive and independently readout. With such a system, we plan to implement two qubit gates between two Kerr-cat qubits: specifically, a noise-bias-preserving CNOT gate [51]. For the work presented here, we address only one of the two chips with microwave drives and the modes from the other chip play the role of spectators. Table II lists a few key design parameters.

The design closely follows the coaxline architecture that includes a seam between the two package pieces for easy assembly and multiplexing [125]. The package structure

consists of two rectangular waveguide cavities designed with lowest box mode at 12.46 GHz for the addressed system and 12.78 GHz for the spectator system. An aperture between the two cavities couples the two spatially separate box modes weakly compared to their detuning, which helps keep the box eigenmodes—and thus strong microwave drives applied to them—spatially separated while still allowing for direct capacitive coupling between the two SNAIL transmons. The aspect ratio of the boxes (tall and narrow) restricts the on-chip eigenmodes from having significant participation in either the seam or the copper bottom piece. The copper bottom piece is necessary (as opposed to aluminum) to allow penetration of magnetic

TABLE II. Summary of device parameters. All design simulations were performed with ANSYS HFSS and black box quantization [123,124] including corrections to Kerr from cubic nonlinearities [88], which follow from similar corrections in lumped-element calculations [58]. All parameters in the lower two sections correspond to the particular flux bias point $\Phi/\Phi_0 = 0.33$ common to all data in this work. “msmt” refers to “measurement”.

Parameter	Value	Method of estimate or measurement
Oscillator dipole capacitance E_C/h	60 MHz	Design simulation
Oscillator number of SNAILS	2	Design
Oscillator SNAIL asymmetry α	0.1	Room temperature resistance msmt
Oscillator inductance of 1 large junction	0.6 nH	Room temperature resistance msmt
Oscillator inductance of 1 small junction	6 nH	Room temperature resistance msmt
Oscillator frequency at $\Phi/\Phi_0 = 0$	6.668 GHz	Two-tone spectroscopy
Oscillator frequency at $\Phi/\Phi_0 = 0.5$	5.815 GHz	Two-tone spectroscopy
External flux bias point Φ/Φ_0	0.33	Two-tone spectroscopy
Oscillator frequency $\omega_a/2\pi$	6.039 GHz	Two-tone spectroscopy
Oscillator cubic nonlinearity $g_3/3/2\pi$	≈ 10 MHz	Design simulation
Oscillator self-Kerr nonlinearity $K/2\pi$	320 kHz	Coherent state refocusing experiment (Fig. 10)
Oscillator single-photon decay time T_1	(20 ± 3) μ s	Standard coherence msmt (with fluorescence readout)
Oscillator Ramsey decay time T_2^*	(2.17 ± 0.05) μ s	Standard Ramsey coherence msmt (with fluorescence readout)
Oscillator Hahn echo decay time T_{2E}	13 μ s	Standard echo coherence msmt (with fluorescence readout)
Readout resonator frequency $\omega_b/2\pi$	8.506 GHz	Direct rf reflection measurement
Readout resonator linewidth $\kappa_b/2\pi$	0.40 MHz	Direct rf reflection measurement
Readout resonator internal linewidth	< 0.04 MHz	Direct rf reflection measurement
Readout to oscillator cross-Kerr $\chi_{ab}/2\pi$	~ 10 kHz	Design simulation
Purcell filter frequency	8.703 GHz	Direct rf reflection measurement
Purcell filter linewidth	25 MHz	Direct rf reflection measurement
Lowest box mode frequency	12.46 GHz	Design simulation
Spectator SNAIL-transmon frequency	6.302 GHz	Two-tone spectroscopy
Capacitive coupling between oscillator and spectator	9.4 MHz	Avoided crossing in two-tone spectroscopy vs flux
Spectator SNAIL-transmon self-Kerr	2.8 MHz	Two-tone spectroscopy
Spectator SNAIL-transmon single-photon decay time	20 μ s	Standard coherence msmt (with fluorescence readout)
Spectator SNAIL-transmon Ramsey decay time	2 μ s	Standard Ramsey coherence msmt (with fluorescence readout)
Spectator to oscillator cross-Kerr	≈ 0.03 MHz	Design simulation
Spectator readout resonator frequency	8.775 GHz	Direct rf reflection measurement
Spectator readout resonator linewidth	0.58 MHz	Direct rf reflection measurement
Spectator Purcell filter frequency	8.890 GHz	Direct rf reflection measurement
Spectator Purcell filter linewidth	14 MHz	Direct rf reflection measurement
Lowest spectator box mode frequency	12.78 GHz	Design simulation
Coupling between lowest box modes	≈ 20 MHz	Design simulation

flux to bias the superconducting SNAIL loops via two small coils mounted within counterbored holes in the copper piece. Despite superconducting aluminum's propensity to reject magnetic fields, the necessary applied field to bias the SNAIL loops at one Φ_0 is similar to the same geometry made entirely of copper; as long as the coil area is smaller than magnetic field's entry hole in the aluminum, the magnetic field lines have a convenient return path back through the same hole implying the presence of the aluminum actually has a *focusing* effect of the field toward the SNAIL loops. This results in independent flux-biasing capabilities for two qubits in a 3D superconducting architecture with field crosstalk of order 10^{-2} .

Each sapphire chip is clamped to two copper posts with beryllium copper clips, and hosts three electromagnetic modes of interest: SNAIL transmon, readout resonator, and Purcell filter. A beryllium copper pin inserted into the cavity defines the readout port and sets the linewidth of the readout resonator and Purcell filter; a second weakly coupled pin serves for the application of all microwave drives.

Focusing on the design of the addressed SNAIL transmon, the design change compared to previous work [48], where the coherent state lifetime saturated at $|\alpha|^2 = 2.6$, is a 20-fold reduction in self-Kerr nonlinearity. We actuated this reduction by moving to a series array of $M = 2$ SNAILs, reducing the SNAIL junction asymmetry parameter [57], and working at a larger magnetic flux bias $\Phi/\Phi_0 = 0.33$ closer to (but not at) the Kerr-free flux point [58]. These changes resulted in coherent state lifetime saturation around $|\alpha|^2 = 10$ in the current device (for $\Delta = 0$). This trend is consistent across multiple (including unpublished) devices; namely, lower self-Kerr K devices attain larger $|\alpha|^2$ before the coherent state lifetime saturates despite lower third-order nonlinearity g_3 . The intuition for this result mirrors a similar intuition as to why SNAIL parametric amplifiers with lower self-Kerr handle more signal power before unwanted saturation effects occur [58,59]. Specifically, although increasing M reduces both g_3 and K , it also increases the maximum number of allowed photons in the nonlinear oscillator, which may be parametrized by $n_{\text{crit}} \approx 15M^2/p^2\varphi_{\text{ZPS}}^2$, where p is the inductive participation ratio of the entire SNAIL array in the electromagnetic mode (see Ref. [88] for derivation). With the intuition backed by experiments that drive-induced heating becomes problematic at some fraction of n_{crit} , we may derive an expected increase in Kerr-cat size (at $\Delta = 0$) at which drive-induced heating becomes problematic:

$$\begin{aligned} |\alpha|^2 &= |\epsilon_2/K| \\ &= |g_3\Pi/K| \\ &\propto M\Pi \\ &\propto M^2. \end{aligned} \quad (\text{C1})$$

In the third line we assumed that $|g_3/K| \propto M$ [58,88] and in the last line that n_{crit} scales the limit on $\Pi \propto M$. From this

simple argument, we conclude that increasing the number of SNAILs to decrease Kerr nonlinearity effectively increases the experimentally achievable cat size.

Keeping in mind that gate speeds are limited by the gap in the excited-state spectrum $4K|\alpha|^2$ and that $K \propto 1/M^2$, gate speeds are independent of the Kerr nonlinearity if the expected $|\alpha|^2$ increase is simultaneously achieved. The exception to this is the Kerr-refocusing gate, which takes time $\pi/2K$ irrespective of $|\alpha|^2$. Generally, the gate fidelity, however, will decrease under this optimization since the cat-state lifetime $T_{YZ} = 1/2|\alpha|^2T_1$. As such, we expect there to be an optimum Kerr nonlinearity for a given application depending on the trade-off between achievable gate speed and noise bias. Improvements in gate design and control techniques will help increase gate speed for a given gap in the excited-state spectrum [109], and thereby will allow designs with less nonlinearity to further increase coherent state lifetime and noise bias.

APPENDIX D: READOUT OF THE SQUEEZED KERR OSCILLATOR

It is critical for our implementation that we do not rely on the ordinary dispersive readout of the superconducting circuit platform. This means that our Kerr cats are prepared, evolved, and detected without relying on standard Fock qubit operations or measurements. This ensures the high performance of a system with a weak *bare* nonlinearity. Instead of using the dispersive coupling of the SNAIL transmon to the readout resonator, we use a parametrically activated readout scheme with a large on-off ratio. The readout is enacted by playing a microwave pulse at the frequency difference in between the squeezed Kerr oscillator frame $\omega_d/2$ and readout resonator at ω_b while the stabilization drive is on. The nonlinear term providing the interaction originates from the SNAIL array that, when activated by a microwave tone of displacement amplitude ξ_{BS} and frequency $\omega_{\text{BS}} = \omega_b - \omega_d/2$, transforms as

$$\begin{aligned} &g_3 \left(\hat{a} + \frac{g_{ba}}{\Delta_{ba}} \hat{b} + \text{H.c.} \right)^3 \\ &\rightarrow g_3 \left(\hat{a} e^{-i\omega_d t/2} + \xi_{\text{BS}} e^{-i\omega_{\text{BS}} t} + \frac{g_{ba}}{\Delta_{ba}} \hat{b} e^{-i\omega_b t} + \text{H.c.} \right)^3 \\ &\approx 6g_3 \frac{g_{ba}}{\Delta_{ba}} (\xi_{\text{BS}} \hat{a} \hat{b}^\dagger + \xi_{\text{BS}}^* \hat{a}^\dagger \hat{b}). \end{aligned} \quad (\text{D1})$$

Here, we have used the RWA to get rid of fast rotating terms in a displaced and rotating frame for \hat{a} . g_3 is the third-order nonlinearity of the SNAILs, g_{ba} is the bare capacitive coupling in between the Kerr oscillator and the readout resonator, \hat{b} is the annihilation operator of the resonator, and $\Delta_{ba} = \omega_b - \omega_a$. The hybridization is given in the dispersive approximation for simplicity. Note, however, that the RWA approximation is unjustified—the detuning

of the readout drive is of order the oscillator frequencies—and higher orders need to be considered. To leading order, their effect is a renormalization of the beam-splitter coupling rate g_{BS} in the effective interaction,

$$g_{\text{BS}}\hat{a}\hat{b}^\dagger + g_{\text{BS}}^*\hat{a}^\dagger\hat{b}, \quad (\text{D2})$$

which is the announced frequency-converting beam-splitter interaction.

When activated in the presence of the stabilization drive, the photons in the squeezed Kerr oscillator displace the readout resonator with a resonant drive strength $\pm g_{\text{BS}}\alpha$, which subsequently radiates into a quantum-limited amplifier chain that we demodulate and monitor with a precision microwave measurement setup at room temperature. For sufficiently weak readout drive strength such that $|g_{\text{BS}}|^2 \ll 2K|\alpha|\kappa_b$, the photons emitted by the oscillator are replenished by the stabilization drive effectively preserving the photon number in the state. These photons should be thought of as displacing the readout resonator by an amount $\beta = \pm i2g_{\text{BS}}\alpha/\kappa_b$, which is conditional on $\hat{a} \approx \pm\alpha$, and thus forcing the cat to collapse into one of its coherent state components. The process enacts then a quantum nondemolition measurement of the quadrature in the Kerr-cat qubit, thus named cat-quadrature readout [48]. For nearly degenerate excited states within the metapotential wells, the readout resonator is similarly displaced conditioned on which well $\pm\alpha$. The readout gains no information on population within each well assuming $\kappa_b \ll 4K|\alpha|^2$, as is the case in our experiment. For excited states outside the metapotential wells, the readout drive is sufficiently off resonance from any transitions such that the readout resonator is not appreciably displaced from its vacuum state.

Writing the Langevin equation for the coupled system and solving for the steady state amplitude in the readout resonator (see Refs. [48,88]), we find, as derived [126] and verified [127] for conditional displacement readout, the voltage signal-to-noise ratio of the measurement, which is the square root of the usual power-defined SNR,

$$\sqrt{\text{SNR}(\tau)} = \sqrt{32\eta} \frac{|g_{\text{BS}}\alpha|}{\kappa_b} \quad (\text{D3})$$

$$\times [\kappa_b\tau - 4(1 - e^{-\kappa_b\tau/2}) + (1 - e^{-\kappa_b\tau})]^{1/2}, \quad (\text{D4})$$

where τ is the square measurement pulse time and η is the quantum efficiency of the entire measurement chain. The expression here assumes the optimal demodulation envelope, as used in the experiment. The experimentally measured SNR may be read from histograms as $\text{SNR} = |I_{+\alpha} - I_{-\alpha}|^2/2\sigma^2$, where $I_{\pm\alpha}$ is the mean in-phase quadrature value for preparation in $|\pm\alpha\rangle$ and σ is the standard deviation of the resultant histogram (cf. main text Fig. 2). Note, all information is aligned to the

in-phase quadrature either by the demodulation envelope or by choosing the readout drive phase such that $\arg(g_{\text{BS}}) = +\pi/2$. Invoking the aforementioned drive strength limitation to prevent leakage to higher excited states, we may bound the SNR as

$$\text{SNR} \propto \frac{|g_{\text{BS}}\alpha|^2}{\kappa_b^2} \kappa_b\tau \ll 2K|\alpha|^3\tau \quad (\text{D5})$$

in the long-time $\kappa_b\tau \gg 1$ limit.

The expression favors large values of the mean photon number $|\alpha|^2$ in the oscillator. This is of technological relevance since obtaining high readout SNR is then consistent with the other two main desiderata for the Kerr-cat qubit: namely, fast gate speed (limited by the gap to the first excited state in the spectrum measured here to scale as $\approx 4K|\alpha|^2$) and large noise bias (found to increase with $|\alpha|^2$ in the decoherence studies presented here).

In Fig. 6, we examine the measurement quality as function of squeezing drive amplitude and readout drive amplitude. To this end, we first calibrate the readout drive amplitude in terms of the induced beam-splitter rate g_{BS} with the experimental pulse sequence of Fig. 6(a). With the squeezing drive off ($\epsilon_2 = 0$), we prepare the Fock qubit on the equator of its Bloch sphere and turn on an uncalibrated readout drive (frequency $\omega_{\text{BS}} = \omega_b - \omega_a$) to pitch the Fock qubit state out the overcoupled port of the readout resonator. This effectively performs a fluorescence readout of the Fock qubit [128], which is of higher fidelity than dispersive readout in this system. An example emitted signal measured via heterodyne detection is shown in Fig. 6(b). In the limit $g_{\text{BS}} \ll \kappa_b$, the emitted field's energy would decay exponentially at rate $4g_{\text{BS}}^2/\kappa_b$, implementing a so-called “ Q switch” on the Fock qubit often used for cooling. However, in our experiment $g_{\text{BS}} \gtrsim \kappa_b$, so the photon swaps back and forth at rate $g_{\text{BS}}/2$ between the Fock qubit and the readout resonator before being emitted out the detection port. Fitting these oscillations (black line) allows us to extract g_{BS} (see Refs. [48,129] for model derivation). Performing this experiment for different readout drive amplitudes, we extract g_{BS} and fit the dependence to a line with no offset [Fig. 6(c)] as expected for this three-wave mixing process.

With readout amplitude calibration in hand, we apply the squeezing drive to assess the quality of readout. As in the main text, we follow the pulse sequence in Fig. 6(d) to repeatedly perform readout with the squeezing drive on to set the mean number of photons in the squeezed Kerr oscillator to $|\alpha|^2 = \epsilon_2/K$ ($\Delta = 0$). We examine three readout metrics for three different squeezing strengths as a function of readout drive amplitude: fidelity in Fig. 6(e), QNDness in Fig. 6(f), and decay time during readout in Fig. 6(g). We calculate the fidelity as $\mathcal{F} = 1 - p(+\alpha|-\alpha) - p(-\alpha|+\alpha)$, where $p(\pm\alpha|\mp\alpha)$ is the probability—as extracted from experimental

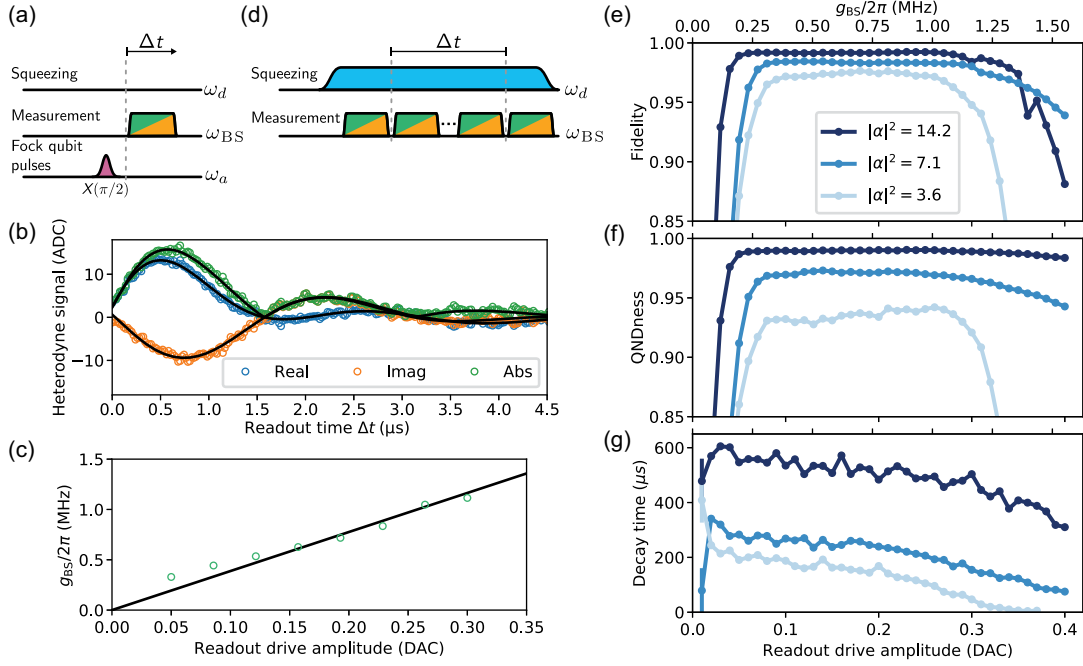


FIG. 6. Measurement calibration and robustness to readout power. (a) Pulse sequence for readout drive amplitude calibration experiment [see (b) and (c)]. Preparing the Fock qubit on the equator of the Bloch sphere (squeezing drive off), a readout pulse at $\omega_{BS} = \omega_b - \omega_a$ implements a fluorescence readout. (b) Example time trace of readout resonator output field recorded as a heterodyne signal after amplification. Black lines are fits to extract beam-splitter strength g_{BS} . (c) Extracted g_{BS} (green circles) as a function of readout pulse amplitude fit to a line (black) with no offset. (d) Pulse sequence for repeated measurement as in main text, where again $\omega_{BS} = \omega_b - \omega_d/2$. (e)–(g) Fidelity, QNDness, and decay time during repeated measurements, respectively, as a function of readout drive amplitude for three different squeezing drive strengths on resonance. Lines connecting points are a guide to the eye.

histograms—of measuring the qubit in $|\pm\alpha\rangle$ after initializing the opposite state $|\mp\alpha\rangle$ with a previous stringently thresholded measurement. We characterize the QNDness as $\mathcal{Q} = [P(+\alpha|+\alpha) + P(-\alpha|-\alpha)]/2$, where $P(i|i)$ is the probability of obtaining measurement outcome i in two successive fair measurements. We extract the decay time-scale during measurement by averaging many measurement records together conditioned on the first initialization measurement and fitting to a single exponential decay (see main text Fig. 2).

Focusing first on the readout drive amplitude dependence, both the fidelity and QNDness increase sharply at low amplitude as the blobs separate in IQ space and the bare SNR increases. For a large region of readout drive amplitude, the fidelity and QNDness are both approximately constant until eventually degrading at higher amplitudes. We interpret the constant region to correspond to the drive amplitudes where the fidelity is no longer limited by the bare SNR of the blob separation, but instead by the decay of one coherent state to the other during readout. This interpretation is consistent with comparing the total time for a single measurement $\tau = 4.44 \mu\text{s}$ to the measured decay time during readout. The measured QNDness also saturates since the maximally extractable QNDness for this experimental definition depends on the readout fidelity. A fidelity-independent way to extract

QNDness is to look at the extracted decay time during readout. The decay time decreases monotonically (ignoring the lowest amplitude points of low QNDness) with increasing readout drive amplitude. This is reminiscent of the same reduction of lifetime during readout with increased readout power—colloquially often referred to as “ T_1 vs \bar{n} ”—that plagues most circuit QED systems [130–132].

Turning to the cat size $|\alpha|^2$ dependence on readout quality, the data clearly indicate increased fidelity, increased QNDness, and increased lifetime during readout for larger $|\alpha|^2$ in the range shown. The reason for this trend is threefold: Increasing $|\alpha|^2$ increases bare SNR [cf. Eq. (D4)], increasing $|\alpha|^2$ increases coherent state lifetime [cf. main text Fig. 3(d) and Appendix G 3], and increasing $|\alpha|^2$ increases robustness to external drives (cf. Fig. 7 in Appendix E). Generally, these trends continue until increasing $|\alpha|^2$ no longer increases the coherent state lifetime T_X , implying that designing systems with larger T_X will correspondingly increase readout performance even in the regime of T_1 -vs- \bar{n} -type effects. Such considerations might lead future experiments to optimize readout performance by always performing readout at the highest T_X bias point. For instance, an application that might wish to set $|\alpha|^2$ lower to optimize the breakeven metric may still wish to inflate $|\alpha|^2$ before readout by increasing e_2 adiabatically with respect to $4K|\alpha|^2$. Without increasing T_X , increasing

readout speed would further increase readout fidelity (in the flat regime of readout amplitude where fidelity is otherwise limited by lifetime). The relatively conservative value of $\kappa_b/2\pi = 0.40$ MHz limited our readout time $\tau = 4.44$ μ s and may be easily increased in future experiments.

APPENDIX E: PRESERVATION OF THE BIAS DURING CONTINUOUS CAT RABI GATE

The metapotential describes a double-well energy surface with nonlinear components in both the x and p quadratures. Regardless, around its minima $\tilde{\alpha}$ a harmonic approximation becomes increasingly good as $\epsilon_2 \gg K$. Defining the operator $\delta\hat{a} = \hat{a} - \tilde{\alpha}$, we use the generalized Taylor expansion for Hilbert space operators to write now the non-Hermitian Hamiltonian Eq. (B6) as

$$\begin{aligned} \hat{H}_{\text{SK}}^{\text{no-j}}/\hbar \approx & -4\tilde{K}|\tilde{\alpha}|^2(\delta\hat{a}^\dagger)\delta\hat{a} - \tilde{K}(\delta\hat{a}^\dagger)^2(\delta\hat{a})^2 \\ & - 2\tilde{K}\tilde{\alpha}(\delta\hat{a}^\dagger)^2\delta\hat{a} + \text{H.c.}, \end{aligned}$$

which stands for an oscillator that becomes stiffer as ϵ_2 grows while its Kerr nonlinearity remains constant. This increasingly harmonic oscillator is described by an energy $\hbar\Delta_{\text{gap}} = -\hbar(4K + i2\kappa_2)|\alpha|^2$. This energy limits the speed of operation of the Kerr-cat qubit and can be thought of as the energy gap in between the degenerate logical space of the qubit and the first level out of the code space. We have reported the experimental verification of this scaling in the case $K \gg \kappa_2$ in the main text. In absence of Kerr nonlinearity ($K \ll \kappa_2$) it has been verified and reported in Ref. [62].

The operation speed limit is discussed in Ref. [48] but can be understood, alternatively, in the following way. The cat Rabi drive, in resonance with $\omega_d/2$ and of amplitude ϵ_x , can be thought of as drive detuned by Δ_{gap} over the stiff harmonic wells of the metapotential. In the presence of single-photon dissipation, such a detuned drive will stabilize, in the harmonic oscillators, a coherent state of amplitude $\epsilon_x/(\Delta_{\text{gap}} - i\kappa_1/2) \approx \epsilon_x/\Delta_{\text{gap}}$. The condition

of perturbative drive is that the displacement of ground state is much smaller than the vacuum spread: $\epsilon_x/\Delta_{\text{gap}} \ll 1$. This condition ensures that the state will not “leak” out of the logical manifold into the excited states and limits the achievable Rabi rate $\Omega_x = \text{Re}\{4\epsilon_x\alpha^*\}$ to $|\Omega_x| \ll 4|\Delta_{\text{gap}}\alpha| = 16|\alpha|^3\sqrt{K^2 + \kappa_2^2}/4$.

We further verify that the coherent state lifetime is not degraded by pushing the rate of the continuous cat Rabi gate toward this limit. In Fig. 7, we observe that even past the largest gap involved in our experiments (~ 12 MHz for $|\alpha|^2 \sim 10$), the coherent state lifetime T_X is essentially unaffected. Naturally, for such high Rabi amplitudes the state undergoes coherent oscillations in between the ground state and the excited states of the metapotential (corresponding to leakage) and should be avoided during the operation of the Kerr-cat qubit. Importantly, at these high amplitudes where the drive is explicitly causing leakage, T_X is unaffected because the leakage is primarily to pairwise degenerate state within the wells. This relaxes constraints on leakage errors during gates in applications that require the preservation of a large noise bias.

APPENDIX F: BOHR QUANTIZATION OF THE SQUEEZED KERR OSCILLATOR

In this appendix, we will treat in a semiclassical fashion the squeezed Kerr oscillator and use Bohr’s quantization principle to find the number of bound states per well. We first take the invertible Wigner transform \mathfrak{W} of the squeezed Kerr Hamiltonian operator in Eq. (2) in the main text. The quantum phase-space Hamiltonian reads [89,90,133–135]

$$H_{\text{SK}}(x, p)/\hbar = \left(K - \frac{\Delta}{2}\right)(x^2 + p^2) \quad (\text{F1})$$

$$- \frac{K}{4}(x^2 + p^2)^2 + \epsilon_2(x^2 - p^2), \quad (\text{F2})$$

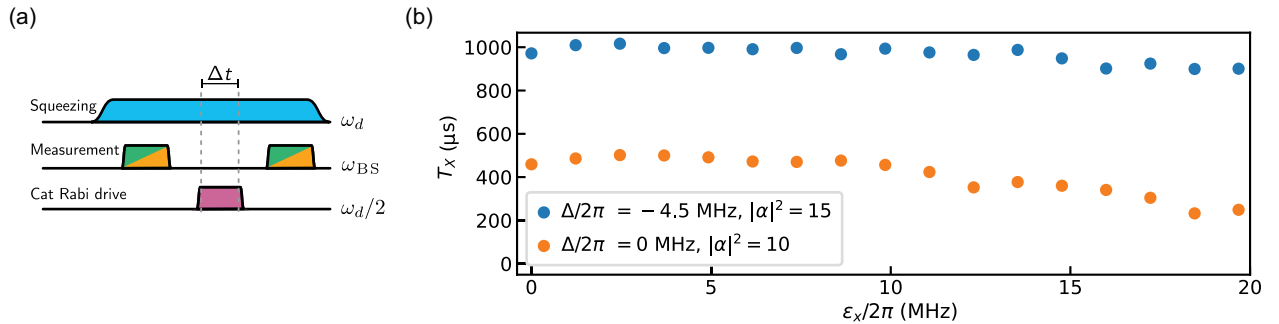


FIG. 7. Bias robustness during gate operation. (a) Pulse sequence to measure T_X in the presence of a strong cat Rabi drive at frequency $\omega_d/2$ with amplitude ϵ_x and phase set to zero to drive cat Rabi oscillations at rate $\Omega_x = \text{Re}\{4\epsilon_x\alpha^*\}$. (b) The coherent state lifetime T_X is unaffected by the strong Rabi drive. The two sets of points corresponds to a coherent state of $|\alpha|^2 = 10$ ($\Delta/2\pi = 0$, orange) and $|\alpha|^2 = 15$ ($\Delta/2\pi = -4.5$ MHz, blue).

where we took $\hat{a} = (\hat{x} + i\hat{p})/\sqrt{2}$ with $[\hat{x}, \hat{p}] = i$ and neglected irrelevant additive constants. The frequency shift $K(x^2 + p^2)$ is the expected McCoy [90,133] correction and it has its origin in the familiar noncommutativity in between \hat{a} and \hat{a}^\dagger . This correction is nothing but the Lamb shift.

Following Dirac's correspondence [136] we take the classical limit " $\hbar \rightarrow 0$ " to transform Eq. (F1) into the fully classical phase-space Hamiltonian:

$$H_{\text{SK}}^{\text{cl}}(x, p)/\hbar = -\frac{\Delta}{2}(x^2 + p^2) - \frac{K}{4}(x^2 + p^2)^2 + \epsilon_2(x^2 - p^2). \quad (\text{F3})$$

As one can see in Fig. 8(a), the equienergy contours defined by $H_{\text{SK}}^{\text{cl}}(x, p) = E$, for $\Delta = 2\epsilon_2$, define trajectories that are Cassinian oval orbits [70]. The separatrix dividing the bound states from the out-of-well states is given by $E = 0$ and describes a figure-8 curve known as Bernoulli's lemniscate. The area enclosed by the teardrop loop can be analytically computed to be

$$\frac{1}{2\pi} \oint_{H_{\text{SK}}^{\text{cl}}=0} P dX = \hbar \left(\frac{\epsilon_2}{\pi K} + \frac{-\Delta}{8K} \right), \quad (\text{F4})$$

where $|\alpha|^2 = \epsilon_2/K$ and X and P are the dimensionated quadratures. Since Bohr's quantization condition reads $(1/2\pi) \oint P dX = \hbar N$, where N is the number of bound states, one finds $N = [(\epsilon_2/\pi K) + (-\Delta/8K)]$. This gives a new rule of thumb to estimate the degree of error protection of the coherent state in the Kerr-cat qubit as a function of its size.

To verify the semiclassical understanding we compare this prediction with a full quantum treatment that we show in Figs. 8(b)–8(d). First, we consider the spectrum of \hat{H}_{SK} [Fig. 8(b)] and define the energy difference $\Delta E_{\text{SK}}^{(n)} = E_{\text{SK}}^{(2n+1)} - E_{\text{SK}}^{(2n)}$ in between pairs of kissing lines. We see [Fig. 8(c)] that $\Delta E_{\text{SK}}^{(n)}$ describe sigmoidal curves. For relatively small $|\alpha|^2$ the energy gap in between excited states remains approximately constant. At critical $|\alpha|^2$ values an exponential degeneration takes place. The inflection point [Fig. 8(d)] at which the rate of approach is maximal defines the kissing point after which the

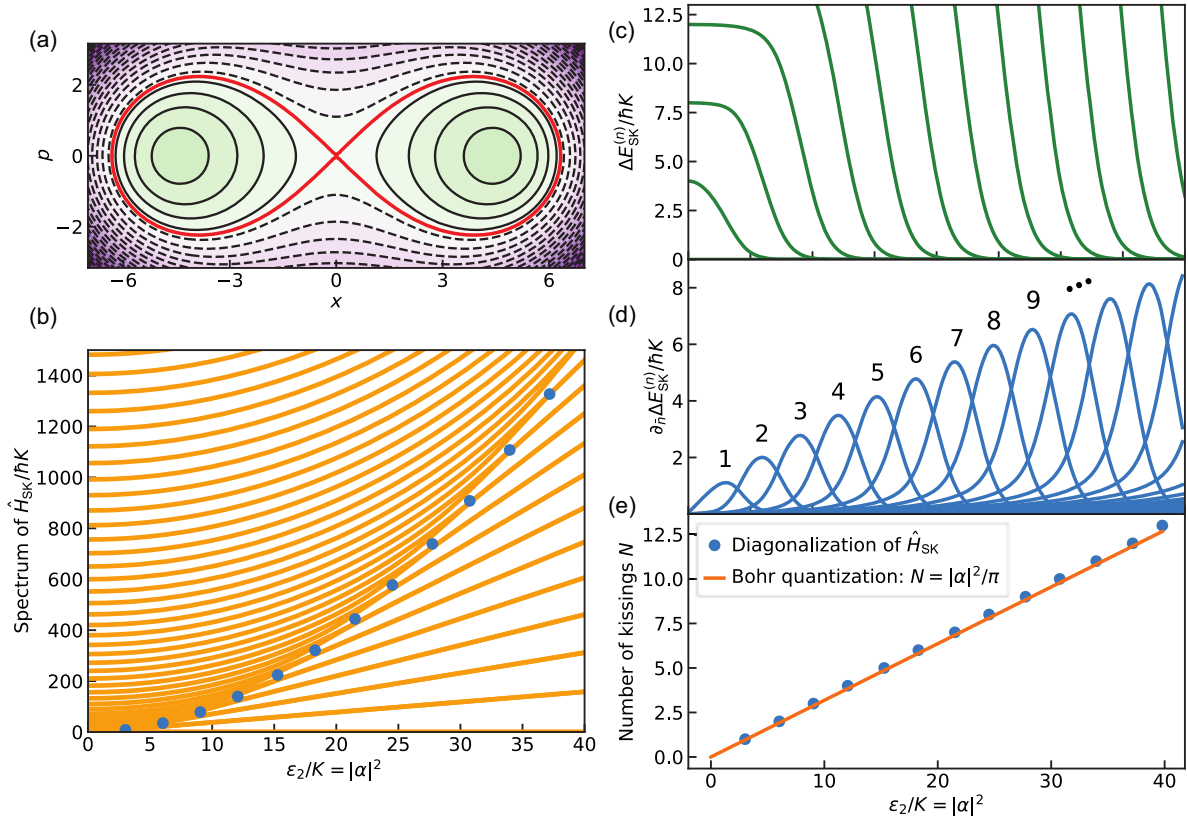


FIG. 8. Bohr quantization of the squeezed Kerr oscillator. (a) Equienergy contours of $H_{\text{SK}}^{\text{cl}}$ describing Cassinian oval orbits, including a lemniscate of Bernoulli (red) taken for $\Delta = 0$. (b) Quantum spectrum of the squeezed Kerr oscillator and (c) the energy gap in between kissing eigenenergies as a function of the squeezing drive amplitude. (d) The point of maximal rate of approach is defined as the kissing point and determined by the inflection point in the energy gaps. These are marked as blue dots in (b). (e) Comparison in between the quantum Hamiltonian treatment and Bohr's quantization semiclassical argument.

marginal splitting left vanishes toward infinity. This defines unambiguously the kissing point. Note, however, that since the approach is so abrupt the argument is largely independent of the exact definition of the kissing point and that any reasonable cutoff imposed over $\Delta E_{SK}^{(n)}$ yields essentially the same result. We compare the fully quantum treatment (for $\Delta = 0$) with the semiclassical argument in Fig. 8(e) to find remarkable agreement.

APPENDIX G: DECOHERENCE IN THE SQUEEZED KERR OSCILLATOR

1. Decoherence for our stabilized Schrödinger cat states

In Fig. 9 we show the coherence damping of Rabi-like fringes while the Kerr-cat qubit oscillates in between the different cat parities as $\mathcal{N}(t)(|\alpha\rangle + e^{i\Omega_x t}|\alpha\rangle)$. This is achieved by applying a resonant drive on the system while the squeezing drive remains on as depicted in Fig. 9(a): The stabilization drive is on during a first QND measurement that is used to prepare a coherent state in the metapotential. The squeezing drive is then turned off

abruptly to perform a Kerr gate [48] and prepare a Yurke-Stoler parityless cat. After free Kerr evolution time of $\pi/2K$ the stabilization drive is turned on again to “catch” the cat state. Then a resonant Rabi drive is applied on the qubit. The stabilization drive frustrates the displacement of the coherent components but causes the interference fringes of the Kerr-cat qubit to roll, changing its parity as it exchanges photons, coherently and one-by-one, with the resonant drive. This is the mechanism used to perform the continuous X gate in the Kerr-cat qubit [48], following a similar gate in dissipatively stabilized cat qubits [62]. The oscillation around the cat meridian of the Kerr-cat qubit Bloch sphere for different values of the squeezing drive amplitude are shown in Fig. 9(b). Since the Rabi dynamics will perform a π pulse every time a “red” cat fringe ($W > 0$; see Fig. 1 in the main text) is displaced to the position previously occupied by a “blue” fringe ($W < 0$), one expects the Rabi frequency to be a strong function of $|\alpha|^2$: As the cat states become larger, their fringes become narrower and a smaller displacement is required to enact the coherent parity flip [137]. By fitting the Rabi frequency $\Omega_x(\alpha)$ we

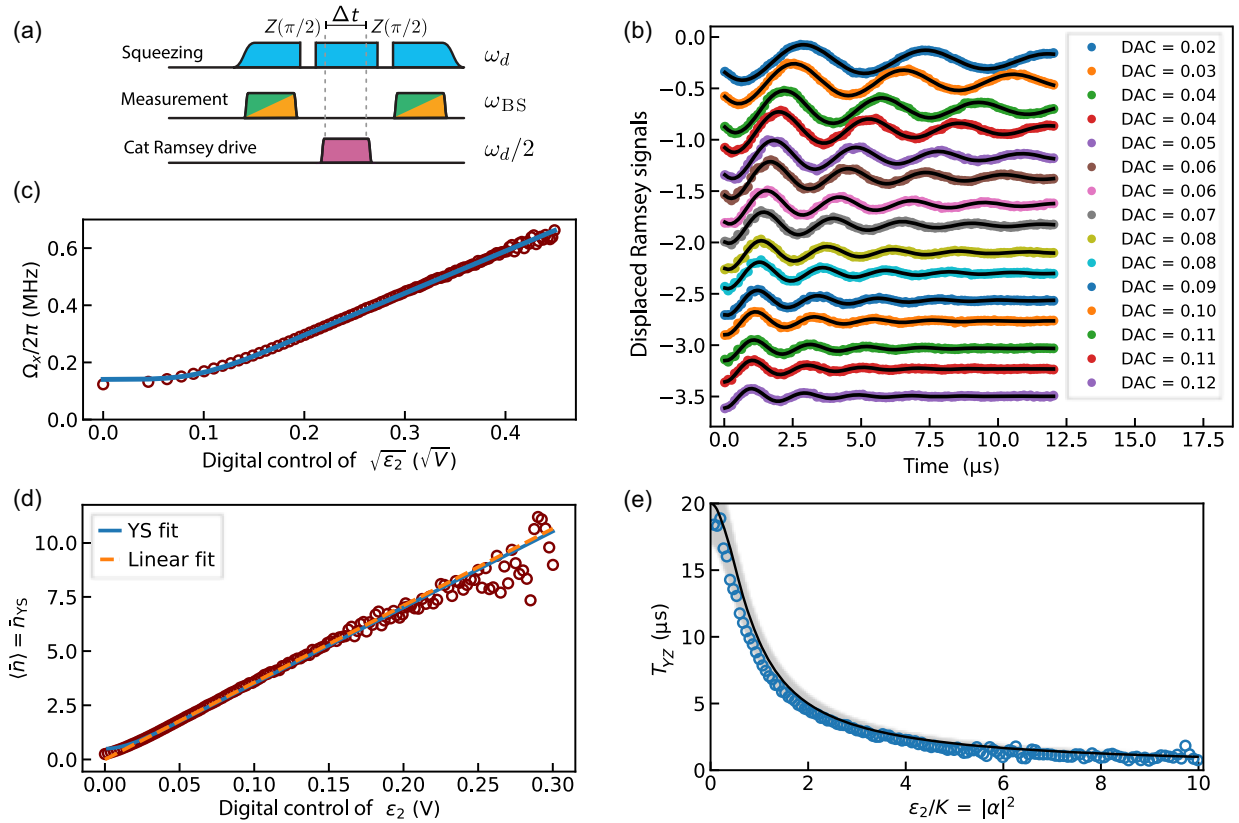


FIG. 9. Cat Rabi as a calibration tool. (a) The experimental sequence used to perform Rabi oscillations in between oscillator states. (b) We show 15 of the 101 cat Rabi oscillations, each for a different squeezing amplitude. The frequency of the oscillation is directly proportional to the square root of the cat size and the decoherence constant is inversely proportional to it. (c) Fit of the cat Rabi frequency as a function of the voltage control parameter. (d) Inverting the formula for the Rabi frequency we measure directly the average number of photons $\langle \bar{n} \rangle$ in the ground state of the metapotential, which is equivalent to average number of photons in the parityless Yurke-Stoler (YS) cats. (e) Measurement of the cat-state lifetime. The solid line is a parameter-free theory prediction with shaded error bars corresponding to the experimental uncertainty on the independently measured single-photon lifetime.

can calibrate the size of the cat as a function of digital control amplitude (DAC) controlling the stabilization drive ϵ_2 .

In the large cat limit, a drive term $\hat{V}_x = \epsilon_x \hat{a}^\dagger + \epsilon_x^* \hat{a}$ breaks the degeneracy in between the even and odd cat states by [48,62]

$$\Omega_x = 2\langle\alpha|\hat{V}_x|\alpha\rangle = \text{Re}(4\epsilon_x\alpha^*) \quad (\text{G1})$$

to first order in perturbation theory.

Extending this simple treatment to be valid for smaller values of $|\alpha|^2$, one gets $\Omega_x \approx \text{Re}(4\epsilon_x\sqrt{\bar{n}_{YS}})$, where we have introduced a notation for the mean number of photons in the parityless cats as $\bar{n}_{YS} = \frac{1}{2}|\alpha|^2(r^2 + r^{-2})$ with r being the ratio of the normalization constants for the even and odd cats as defined in Eq. (B2). The extension of this formula relies on the fact that the parityless cats map naturally to the equatorial superposition of the Fock-state Bloch sphere, while at large values of α the difference in photon number for different cats is vanishingly small. The maximal photon-number difference is in between the even and odd cat states and reads $(\bar{n}_+ - \bar{n}_-) \rightarrow -4|\alpha|^2 e^{-2|\alpha|^2}$ in the limit of large $|\alpha|^2$. In Fig. 9(c) we show the fit of the data with the generalized formula. The inverse of the same formula is used to calibrate directly the cat size of the Hamiltonian ground state as a function of the digital control amplitude for the squeezing drive as shown in Fig. 9(d). As expected, the dependency becomes linear already at fairly low values of $|\alpha|^2$.

It is clear that the oscillations shown in Fig. 9(b) are not fully coherent. Indeed, their increasing decay rate with $|\alpha|^2$ is a characteristic of Schrödinger cat states and a signature of the quantum to classical transition [138]. In Fig. 9(e) we show the measured coherence time of the cat states for different values of $|\alpha|^2 = \epsilon_2/K$. Since in a Kerr-cat Bloch sphere with a given α the mean photon number of the cat states is only the same if $|\alpha|^2 \gtrsim 1$, measuring the Rabi-like damping of the Kerr-cat Rabi oscillations (instead of monitoring the exponential relaxation of a cat with a given parity) provides us with an effective damping rate representative of the encoding, which we refer to as T_{YZ} . The dots are experimental data and the lines are independently calibrated theory plots. The solid line represents the parameter-free curve $T_{YZ} = T_1/2\langle\bar{n}\rangle$, where $\langle\bar{n}\rangle$ is the Bloch-sphere-average photon number around the cat meridian and reads $\langle\bar{n}\rangle = \bar{n}_{YS}$. The dashed lines represent the uncertainty in the independently measured transmon lifetime $T_1 = (20 \pm 3) \mu\text{s}$.

2. Decoherence of q -legged cats during free Kerr evolution (the Kerr gate)

During the Kerr gate [48] the state evolves under the native (undriven) Kerr Hamiltonian of the system. Turning

off abruptly the squeezing drive, which stabilized the cat manifold, enacts a Yurke-Stoler evolution [139] transforming the state from a coherent state into a two-legged parityless cat state after a time $t = \pi/2K$. It is interesting to notice that the system visits a series of intermediate q -legged cat states every $t = \pi/qK$ [138]. These multi-legged cats exhibit a complex pattern of interference fringes in phase space and their sharp phase-space features exposes them to accentuated diffusion under dissipation. This makes the fidelity of the Kerr gate a strong function of the mean photon number, and thus a sensitive tool to study the decoherence in our system. It is important to note that the high-frequency variation in the Wigner distribution of q -legged cat states is set by the square of their phase-space diameter ($D = 2\sqrt{\bar{n}}$).

We here study experimentally the decoherence during the free Kerr evolution as a function of the cat size $|\alpha|^2$. Our measurement configuration allows us to easily access the mean value of the Kerr-cat qubit Pauli operator $\hat{X} \approx |+\alpha\rangle\langle+\alpha| - |-\alpha\rangle\langle-\alpha|$ [see Eq. (B4)]. The experimental measurement sequence is shown in Fig. 10(a). A preparation QND measurement performed in the presence of the stabilization drive is followed by a period of free Kerr evolution before the final measurement is performed. The experimental results are shown in Fig. 10(b). We see that at the time of the phase refocusing π/K the degree of coherence decreases rapidly with the photon number up to the point that the state is largely dephased. By that time, the phase-space distribution is expected to be essentially classical. The solid black line is a fit via simulation of a master equation including only single-photons loss. Including photon excitation in the simulation with a free thermal photon number as an additional free parameter achieves the same goodness of fit at the cost of a high uncertainty in the fit parameters. We thus exclude it from the analysis here. We find that a correct interpretation of the data is achieved by understanding $\kappa_{\text{eff}} \sim \kappa_1(1 + 2n_{\text{th}})$ as verified numerically. The fitted parameters are shown in Figs. 10(c)–10(e).

By giving the fit function complete freedom over the Hamiltonian parameters K and ϵ_2 , we find that only a modulation of $\sim 3\%$ is required to reproduce the complex free Kerr evolution for all values in a large range of $|\alpha|^2$. Moreover, we see from Fig. 10(c) that fitted values are consistent with independently performed calibrations discussed in the previous section and in the main text. We notice that in the free Kerr experiment the Kerr coefficient has a slight decreasing trend as the size of the cat states grows. As expected for larger values of $|\alpha|^2$, the refocusing signal becomes weaker. We see nonetheless a significant increase in the effective decoherence rate of $\sim 200\%$ making $2\bar{n}T_Y < T_1 = \kappa_{\text{eff}}^{-1}$. The fitted value for κ_{eff} is compatible with $\kappa_1 = 1/20 \mu\text{s}$ and $n_{\text{th}} \sim 0.3$ for $|\alpha|^2 < 4.9$.

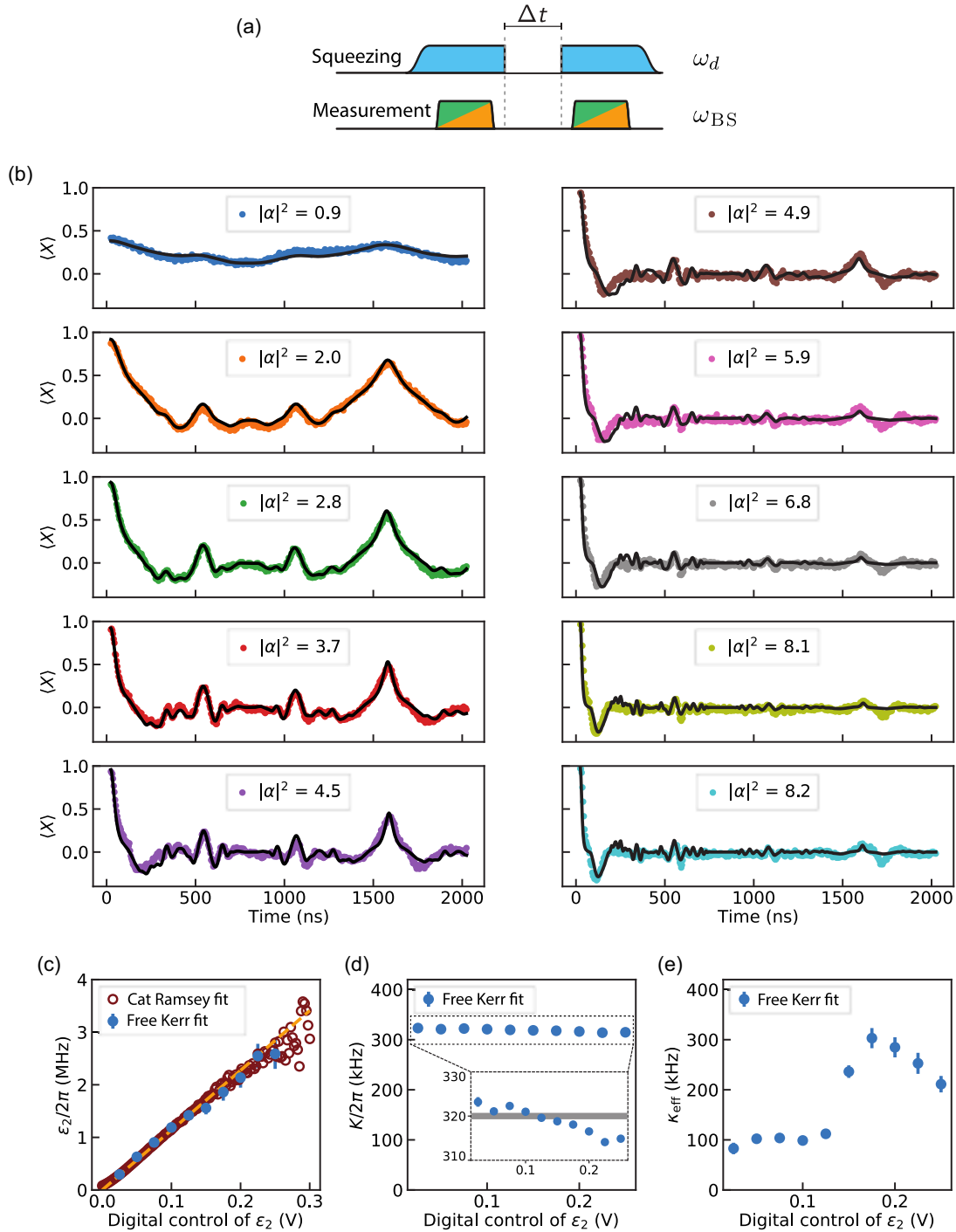


FIG. 10. The Yurke and Stoler experiment as a calibration tool. (a) The experimental sequence of pulses allowing for the observation of the phase collapse and the phase revival in free Kerr oscillator. At times equal to π/qK the system is in a q -legged Schrödinger cat state. (b) The signal corresponds to the mean value of the operator $\hat{X} \approx |+\alpha\rangle\langle+\alpha| - |-\alpha\rangle\langle-\alpha|$ [cf. Eq. (B4)] achieving maximal revival at π/K . For large cats the periodicity of the signal is lost due to decoherence (see Ref. [140]). (c) Fitting the cat size over the free Kerr evolution signal provides an efficient calibration of the drive parameters which is consistent with that obtained from the cat Rabi experiments discussed in Fig. 9. (d) The revival is expected at π/K independently of the cat size and thus fitting the signals in (b) provides a good calibration for the Kerr parameter K . It is found to be $K \sim 320$ kHz in agreement with independently performed spectroscopic experiments (see main text). (e) The fitted effective dissipation rate as a function of the cat size. We find a nontrivial dependence on the dissipation rate for larger cats. This suggests an effective heating of the setup for the larger squeezing amplitudes.

3. Decoherence of stabilized coherent states

The most striking result regarding the interplay of nonlinearity and decoherence in our work is the experimental discovery of a stepped increase in the coherent state lifetime versus the mean photon number in the logical state. This showcases the interplay in between nonlinearity and dissipation and the relevance of the excited-state structure in our system to the error correcting properties of our qubit implementation. Every time that the quantity $|\alpha|^2/\pi$ hits an integer value the Kerr-cat qubit earns one more order of error protection. This is a direct consequence of the vanishing tunnel splitting as excited states sink into the wells of the metapotential and under the barrier. The qualitative effect over the decoherence in the system is largely independent of the specific error channels considered: A staircase in the lifetime is expected. On the other hand, quantitative predictions do depend on the dominating error channel at play. We here discuss how some of the main features of decoherence of our coherent states can be explained by a simple model keeping RWA terms in the coupling to the environment which contains single-photon loss ($\kappa_1(1+n_{\text{th}})\mathcal{D}[\hat{a}]$), thermal excitations ($\kappa_1 n_{\text{th}}\mathcal{D}[\hat{a}^\dagger]$), and detuning-type noise ($\kappa_\phi\mathcal{D}[\hat{a}^\dagger\hat{a}]$). A non-Markovian contribution motivated by highly correlated magnetic flux noise threading the superconducting SNAIL loops is also included.

We first provide a numerical model including single-photon loss, thermal excitations, dephasing, and non-Markovian low-frequency detuning noise. We then provide

an analytical model to showcase the importance of the excited level spectrum, which we restrict to single-photon loss and thermal excitations for brevity.

A beyond-RWA Lindbladian model that explains quantitatively the data by deriving from first principles a set of exotic dissipators created by the interplay of nonlinearity and dissipation will be presented elsewhere.

RWA Lindbladian evolution. In Figs. 11(a) and 11(b) we show Markovian master equation simulations considering single-photon loss and a bath at constant temperature for two different magnitudes of *white* dephasing noise (κ_ϕ). Here the colored dots are numerical simulation and the lines are a guide to the eye. The base temperature of our fridge is close to 30 mK but the radiation environment is believed to be at a higher temperature [48]. A thermal population of $n_{\text{th}} \sim 0.05$ was used as a lower bound since it corresponds to a blackbody temperature at ~ 6 GHz of 100 mK, which is pessimistic for superconducting circuits ($n_{\text{th}} \sim 0.1$ corresponds to ~ 120 mK). In this oversimplified model, the temperature is scanned maintaining the single-photon lifetime fixed at ~ 20 μs . In view of the expected $1/f$ dependence of the flux noise, the computations in absence of dephasing noise is only a heuristic. We represent high-frequency flux noise that causes leakage with an effective white noise strength κ_ϕ .

In all our simulations we observe a marked inflection point at $|\alpha|^2 \sim 2\pi$ and $|\alpha|^2 \sim 3\pi$ as expected from Bohr's phase-space quantization (see Appendix F). The first-order

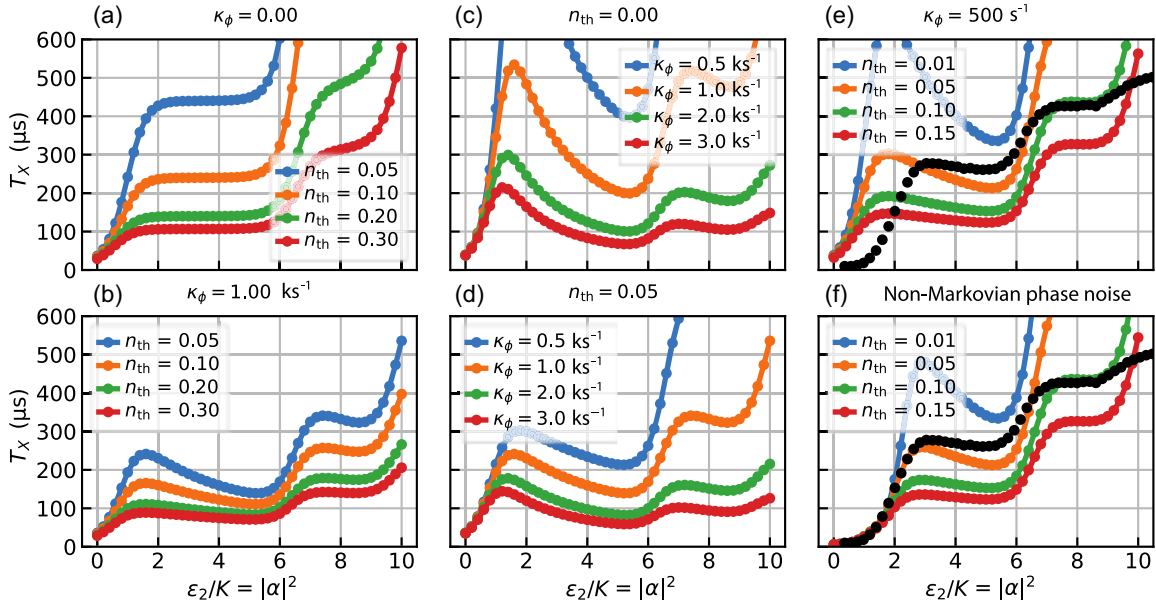


FIG. 11. (a) Numerical simulations in absence of phase noise ($\kappa_\phi = 0$) for a set of different thermal populations. The steps in the coherence state lifetime originated by the discretization of phase-space orbits are apparent. (b) The lifetime study is performed in presence of white phase noise for a range of temperatures keeping the coherent state lifetime in the region of interest. (c) The lifetime study is performed in absence of thermal photons for a set of white phase-noise amplitudes. (d) For a given temperature, the effect of different phase-noise amplitude is compared. (e) Experimental data compared with a sample of Markovian noise models. (f) The low $|\alpha|^2$ behavior of the data is reproduced by a non-Markovian toy model including low-frequency components in the fluctuations of the Hamiltonian term $\Delta\hat{a}^\dagger\hat{a}$ [see Eq. (1) in the main text].

protection happening at $|\alpha|^2 \sim \pi$ presents itself as a subtle inflection point. This is due to the fact that for small values of $|\alpha|^2$ ($\lesssim 1$) the limiting factor is not thermal excitation to the first excited state. Instead, the limiting factor originates from the fact that the Hamiltonian wells are not sufficiently distant in phase space for the states $|\pm X\rangle$ to be well approximated by coherent states; the metapotential wells do not yet contain enough area to host two nonoverlapping states. As such, single-photon loss and dephasing still dominate the decoherence for $|\alpha|^2 \lesssim \pi$. Additionally, due to this lack of separation, coherent and incoherent tunneling represented by residual no-jump Hamiltonian terms $-(\Delta + i\kappa_1/2)\hat{a}^\dagger\hat{a}$ is not yet sufficiently suppressed. In this regime decoherence is also facilitated by errors in the calibration of the drive frequencies, slow fluctuations of the resonance condition in the setup, and by deterministic ac Stark shifts over the SNAIL's oscillator frequency due to the stabilization drive. These types of effect for nonzero effective detuning have been studied theoretically in Ref. [29] and explained via the WKB approximation as the opening up of phase-space tunneling channels in between the wells. An in-depth experimental study of these physics in our system is left for a future work. We here restrict to the observation that these tunneling effects are suppressed in the Kerr-cat regime entered as $|\alpha|^2 > 1$ [75].

We see that in absence of Markovian dephasing noise ($\kappa_\phi = 0$) the plateaus are rather flat, while for $\kappa_\phi > 0$ they contain a downward slope that we recognize in our data. This downward trend implies a degradation of the coherence during the intervals where the mean photon number grows but the increase in area of the limiting orbit is not sufficient to host a new excited pair of levels. A steep increase is then observed when the Bohr's quantization condition is fulfilled. This behavior is expected analytically from the photon-number dependence of the dissipators associated with photon loss (or gain) and the one causing detuning errors. The imaginary operator contribution of each of the involved dissipators to the no-jump non-Hermitian Hamiltonian is either $\propto |\alpha|^2$ or $\propto |\alpha|^4$, respectively (see Table I).

In Figs. 11(c) and 11(d), we plot the behavior for a few values of κ_ϕ at given sample temperatures. From Fig. 11(c), we learn that phase noise by itself cannot explain the qualitative behavior of our data, even if we allow for a monotonic parametrization of κ_ϕ as a function of $|\alpha|^2$. This would represent the approximation of in-band white noise at a single relevant frequency. From Fig. 11(d), we see that a finite temperature limits the coherent state lifetime before the first-order protection peak is achieved, but the value consistent with this saturation fails to control the lifetime at larger values of $|\alpha|^2$. Larger values of κ_ϕ that control the lifetime at $|\alpha|^2 \sim 10$ fail instead to reproduce the experimentally observed value of saturation at $|\alpha|^2 \sim \pi$.

In Figs. 11(e) and 11(f), we reproduce the experimental data as black dots on top of numerical computations for the expected lifetime under different decoherence models. In Fig. 11(e), we reproduce a choice of Markovian models including single-photon gain, single-photon loss, and a $\kappa_\phi = 500 \text{ s}^{-1}$. We see that, in the center region of the plot, it is possible to assign a temperature to the measurement, but the choice becomes inconsistent at either low or high values of $|\alpha|^2$. At the high end of $|\alpha|^2$, we see what may be interpreted as an increased effective heating as the data traverse different isotherms. This is consistent with the observations made during the discussion of the free Kerr evolution and suggests that an effective heating is present at larger cat sizes.

The delayed growth of the measured coherent state lifetime for $|\alpha|^2 < 2$ in comparison with the Lindbladian simulations suggests noise sources beyond the Markov approximation. This is confirmed experimentally by applying a spin-echo sequences over the Fock qubit that produced an increase from $T_2^* \sim 2 \mu\text{s}$ to $T_{2E} \sim 13 \mu\text{s}$ and reveals correlated noise in the experiment. A model for the noise relying on the assumption that the tunneling oscillations caused by $\Delta < 0$ are close to critically damped seems to explain well our observations [see Fig. 11(f)]. To mimic this behavior, we take the oscillator frequency from a random normal distribution and average over many realizations of the noise. The frequency fluctuations required to match the experiment ($\sim 10 \text{ kHz}$) are below the spectroscopic linewidth resolution of the fundamental frequency of our SNAIL transmon. As expected [48,75,88], this effect becomes unimportant for $|\alpha|^2 \gtrsim 1$, which is the Kerr-cat operation regime.

In our setup, measurements can be reliably made for $|\alpha|^2 \gtrsim 20$, and a decrease in the coherent state lifetime is observed beyond $|\alpha|^2 \gtrsim 10$. For illustrative purposes, we mention that the RWA Lindbladian models would suggest that for $|\alpha|^2 \sim 25$ the lifetime of the coherent state in our system should be $\sim 50 \text{ min}$ in realistic conditions. These results were obtained in absence of dissipative two-photon stabilization [63] which would, theoretically, provide yet another large improvement factor.

RWA Lindbladian spectrum. We here elaborate a simplified ($\kappa_\phi = 0$) treatment with the objective of developing further the relationship between the nonlinear spectrum of the Lindbladian and the decoherence properties of the system. This study is based on the fact that the lifetimes of excitations above the equilibrium states are obtained from the real part of the corresponding eigenvalue of the Lindbladian superoperator. This identification provides a fully quantum interpretation of the experimentally observed steps in the coherent state lifetime of our system, if still only qualitatively.

Diagonalization of the Lindbladian superoperator. We begin this analysis by introducing the notation for the spectrum of the resonantly squeezed ($\Delta = 0$) Kerr

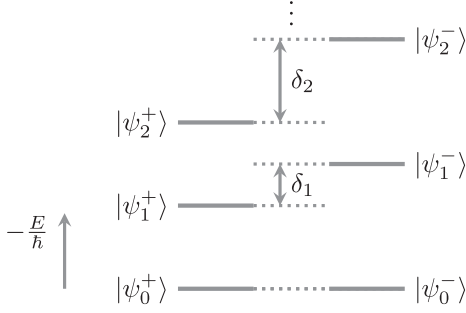


FIG. 12. Tunnel splitting for \hat{H}_{SK} . $|\psi_0^+\rangle$ and $|\psi_0^-\rangle$ are exactly degenerate. The n th excited-state manifold has tunnel splitting $\delta_n \equiv \delta_{nn}^+ = \omega_n^+ - \omega_n^- < \delta_{n+1}$.

Hamiltonian Eq. (2): $\hat{H}_{\text{SK}}|\psi_n^\pm\rangle = \hbar\omega_n^\pm|\psi_n^\pm\rangle$. We choose the eigenstates $|\psi_n^\pm\rangle$ to have overall real expansion coefficients in the Fock basis. For $n = 0$ we have the degenerate cat-state manifold $|\psi_0^\pm\rangle = |\mathcal{C}_\alpha^\pm\rangle$. We denote the energy differences by $\delta_{nm}^{jk} = \omega_n^j - \omega_m^k$ ($j, k = \pm$). Here, $\delta_n = \delta_{nn}^+$ is the tunnel splitting in between the even and odd parity states in the n th excited manifold in the well (see Fig. 12) and decreases exponentially with $|\alpha|^2$ after the kissing point, whereas the out-of-manifold energy gap $\delta_{n,n+1}^{jk} \approx 4K|\alpha|^2$ increases linearly.

Now we provide a physical interpretation of the eigenvalues of the Lindbladian superoperator. Under single-photon loss and single-photon gain, the Lindbladian that governs the evolution of the density operator is

$$\begin{aligned} \mathcal{L} &= \mathcal{L}_H + \mathcal{L}_D, & \mathcal{L}_H \bullet &= \frac{1}{i\hbar} [\hat{H}_{\text{SK}}, \bullet], \\ \mathcal{L}_D \bullet &= \kappa_1 (1 + n_{\text{th}}) \mathcal{D}[\hat{a}] \bullet + \kappa_1 n_{\text{th}} \mathcal{D}[\hat{a}^\dagger] \bullet. \end{aligned}$$

Here κ_1 is the rate of single-photon loss to the environment and n_{th} is the average number of thermal photons. Then the lifetime of the longest-lived excitation is $T_X = [-\text{Re}(\lambda)]^{-1}$, where λ is the eigenvalue of \mathcal{L} with the smallest nonzero real component. In Fig. 13(a), we show the lifetime obtained from the eigenvalue of \mathcal{L} is in agreement with that extracted from exponential fits (dots) of the time evolution, obtained as explained in the previous section from numerical time evolution of the master equation (see Fig. 11).

First-order perturbation theory. We carry the analysis further by exploiting the condition $\kappa_1/K, n_{\text{th}} \ll 1$. In absence of dissipation, the Lindbladian reduces to \mathcal{L}_H , whose eigenoperators are $|\psi_n^j\rangle\langle\psi_m^k|$ with eigenvalues $-i\delta_{nm}^{jk}$ directly determined by the energy differences. The differences are zero for all population eigenoperators $|\psi_n^\pm\rangle\langle\psi_n^\pm|$ and cat-state manifold coherence eigenoperators $|\psi_0^\pm\rangle\langle\psi_0^\mp|$. We now treat dissipation as a perturbation to the unitary dynamics generated by \mathcal{L}_H . Moreover, we observe that a truncation of the Lindbladian can be performed because the eigenoperators corresponding to $\delta_{nm}^{jk} \gtrsim \kappa_1$ do not contribute to the first-order perturbative expansion. That is to say that (i) we exclude out-of-manifold coherence eigenoperators $|\psi_n^j\rangle\langle\psi_m^k|$, where $\delta_{n,m \neq n}^{jk} \sim 4K(n-m)|\alpha|^2 > \kappa_1$, (ii) we exclude the non-degenerate in-manifold coherence eigenoperators $|\psi_n^j\rangle\langle\psi_n^{k \neq j}|$ when their tunnel splittings have not reached the kissing point and $\delta_{nn}^+ \equiv \delta_n > \kappa_1$, whereas (iii) we keep the population eigenoperators $|\psi_n^\pm\rangle\langle\psi_n^\pm|$ because they correspond to zero energy difference, and (iv) we keep the pairs of sufficiently degenerate in-manifold coherence eigenoperators $|\psi_n^\pm\rangle\langle\psi_n^\mp|$ corresponding to $\delta_n < \kappa_1$. In summary, at a fixed value of

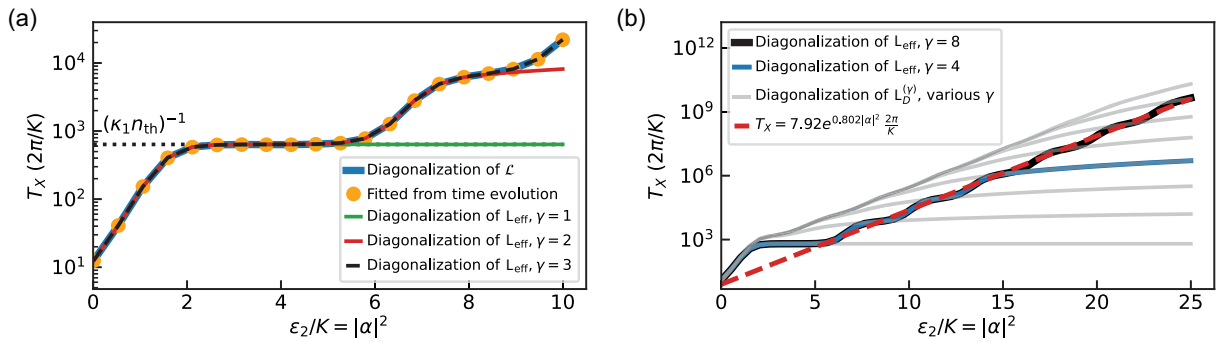


FIG. 13. Spectral fingerprint of the RWA Lindbladian on the coherent state lifetime. (a) Comparison between exact and approximate coherence time of $|X\rangle$ using \mathcal{L} and $\mathbf{L}_{\text{eff}}^{(\gamma)}$. Orange dots: coherence time extracted from Lindbladian time evolution initialized in state $|X\rangle\langle X|$. Solid blue line: $[-\text{Re}(\lambda)]^{-1}$ where λ is the eigenvalue of \mathcal{L} with the smallest nonzero real part. Solid green line: $[-\text{Re}(\tilde{\lambda})]^{-1}$ where $\tilde{\lambda}$ is the eigenvalue of the $2\gamma \times 2\gamma$ matrix $\mathbf{L}_{\text{eff}}^{(\gamma)}$ with the smallest nonzero real part, and $\gamma = 1$. Solid red line: $\gamma = 2$. Dashed black line: $\gamma = 3$. (b) Comparison of $T_X^{(\gamma)}$ in presences and absences of tunnel splittings. The lifetime in the absences of tunnel splittings is derived from $\mathbf{L}_D^{(\gamma)}$. Black line: extracted from $\mathbf{L}_{\text{eff}}^{(\gamma)}$ with $\gamma = 8$. Blue line: with $\gamma = 4$. Gray lines: extracted from $\mathbf{L}_D^{(\gamma)}$ with $\gamma = 1, 2, 3, \dots, 8$ from bottom to top. In both figures, $\kappa_1/K = 0.025$ and $n_{\text{th}} = 0.01$. Red dashed line: fit of the black line restricted to $|\alpha|^2 > 6$.

$|\alpha|^2$ the number of tunnel splittings that satisfy $\delta_n < \kappa_1$ is γ , which is a function of both $|\alpha|^2$ and κ_1 . We then restrict the treatment to the quasidegenerate subspace $\mathcal{B} = \mathcal{B}_{\text{pop}} \cup \mathcal{B}_{\text{coh}}^{(\gamma)}$, where

$$\begin{aligned} \mathcal{B}_{\text{pop}} &= \{|\psi_n^+\rangle\langle\psi_n^+|, |\psi_n^-\rangle\langle\psi_n^-|, \dots, \text{where } n \geq 0\}, \\ \mathcal{B}_{\text{coh}}^{(\gamma)} &= \{|\psi_n^+\rangle\langle\psi_n^-|, |\psi_n^-\rangle\langle\psi_n^+|, \dots, \text{where } 0 \leq n < \gamma\}. \end{aligned}$$

To further reduce the problem, we consider the initial state $\rho(0) = |X\rangle\langle X|$ [where we remind $|\pm X\rangle \equiv (1/\sqrt{2})(|C_\alpha^+\rangle \pm |C_\alpha^-\rangle)$], which can be written as

$$\begin{aligned} \rho(0) &= \frac{1}{2}(|\psi_0^+\rangle\langle\psi_0^+| + |\psi_0^-\rangle\langle\psi_0^-|) \\ &\quad + \frac{1}{2}(|\psi_0^+\rangle\langle\psi_0^-| + |\psi_0^-\rangle\langle\psi_0^+|). \end{aligned}$$

The first term belongs to the subspace \mathcal{B}_{pop} and closely approximates the sole steady state of the Lindbladian. Thus we expect any change in ρ to result from variations in the second term which belongs to $\mathcal{B}_{\text{coh}}^{(\gamma)}$. In addition, under perturbations proportional to $\mathcal{D}[\hat{a}]$ and $\mathcal{D}[\hat{a}^\dagger]$ population and coherence operator subspaces are decoupled under the Lindbladian, due to parity. These two observations allow us to restrict to the 2γ -dimensional subspace $\mathcal{B}_{\text{coh}}^{(\gamma)}$, which we rewrite in the following order:

$$\begin{aligned} \mathcal{B}_{\text{coh}}^{(\gamma)} &= \{|\psi_0^+\rangle\langle\psi_0^-|, |\psi_1^+\rangle\langle\psi_1^-|, \dots, |\psi_{\gamma-1}^+\rangle\langle\psi_{\gamma-1}^-|; \\ &\quad |\psi_0^-\rangle\langle\psi_0^+|, |\psi_1^-\rangle\langle\psi_1^+|, \dots, |\psi_{\gamma-1}^-\rangle\langle\psi_{\gamma-1}^+|\}. \end{aligned}$$

We thus construct the effective Lindbladian matrix $\mathbf{L}_{\text{eff}}^{(\gamma)} = \mathbf{L}_H^{(\gamma)} + \mathbf{L}_D^{(\gamma)}$ with the elements of \mathcal{L} in $\mathcal{B}_{\text{coh}}^{(\gamma)}$ as

$$\begin{aligned} \mathbf{L}_H^{(\gamma)} &= \begin{pmatrix} -\mathbf{\Delta} & \mathbf{0} \\ \mathbf{0} & \mathbf{\Delta} \end{pmatrix}, \\ \mathbf{L}_D^{(\gamma)} &= \kappa_1(1 + n_{\text{th}}) \begin{pmatrix} -\mathbf{A} & \mathbf{B} \\ \mathbf{B} & -\mathbf{A} \end{pmatrix} \\ &\quad + \kappa_1 n_{\text{th}} \begin{pmatrix} -\mathbf{A} - \mathbf{I} & \mathbf{B}^T \\ \mathbf{B}^T & -\mathbf{A} - \mathbf{I} \end{pmatrix}, \end{aligned}$$

where $\mathbf{\Delta}$, \mathbf{A} , and \mathbf{B} are $\gamma \times \gamma$ matrices whose entries depend on $|\alpha|^2$ only:

$$\begin{aligned} \mathbf{\Delta} &= \begin{pmatrix} 0 & & & \\ & i\delta_1 & & \\ & & i\delta_2 & \\ & & & \ddots \end{pmatrix}, \\ \mathbf{A} &= \begin{pmatrix} A_0 & & & \\ & A_1 & & \\ & & A_2 & \\ & & & \ddots \end{pmatrix}, \\ \mathbf{B} &= \begin{pmatrix} B_{00} & B_{01} & B_{02} & \cdots \\ B_{10} & B_{11} & B_{12} & \cdots \\ B_{20} & B_{21} & B_{22} & \cdots \\ \vdots & \vdots & \vdots & \ddots \end{pmatrix}, \\ \delta_n &= \omega_n^+ - \omega_n^-, \\ A_n &= \frac{1}{2}(\langle\psi_n^+|\hat{a}^\dagger\hat{a}|\psi_n^+\rangle + \langle\psi_n^-|\hat{a}^\dagger\hat{a}|\psi_n^-\rangle), \\ B_{mn} &= \langle\psi_m^-|\hat{a}|\psi_n^+\rangle\langle\psi_n^-|\hat{a}^\dagger|\psi_m^+\rangle. \end{aligned}$$

The first-order approximation to the coherent state lifetime is then $T_X \approx T_X^{(\gamma)} = [-\text{Re}(\lambda^{(\gamma)})]^{-1}$, where $\lambda^{(\gamma)}$ is the eigenvalue of $\mathbf{L}_{\text{eff}}^{(\gamma)}$ with the smallest real component. In Fig. 13(a) we plot $T_X^{(\gamma)}$ as a function of $|\alpha|^2$ for $\kappa_1/K = 0.025$ and $n_{\text{th}} = 0.01$. While the level of truncation γ , as defined, should vary with $|\alpha|^2$, we here show the full span for different fixed values of γ . We see, then, that each stepped increase in the coherent state lifetime T_X can be associated to an excited-state manifold; truncating at a particular value of γ amounts to the assumption that $\delta_{n>\gamma} \gg \kappa_1$. Thus, the tunneling associated to states with $n > \gamma$ is considered immediate, and $T_X^{(\gamma)}$ only approximates well T_X if the number of degenerate levels ($N \approx |\alpha|^2/\pi$) is $\lesssim (\gamma + 1)$. If instead $|\alpha|^2 > \pi(\gamma + 1)$, $T_X^{(\gamma)}$ plateaus and informs the rate of excitation outside of the first 2γ states considered in the truncation.

To further illustrate the role of the tunnel splittings in T_X enhancement, we set $\mathbf{L}_H^{(\gamma)} = 0$ and plot the lifetime extracted from \mathcal{L}_D as gray curves in Fig. 13(b). The double-well structure is thus encoded only in the unperturbed eigenbases. The first observation we make is that stepped increase in lifetime vanishes in absence of the kissing spectrum. Secondly, we observe that for $|\alpha|^2$ smaller than the kissing point of the manifold $n = \gamma$ [$|\alpha|^2 < \pi(\gamma + 1)$], the tunneling due to finite splitting in the manifold $n = \gamma$ is a limiting factor for the lifetime [92,93]. Finally, we observe that the exponential trend shown by the lifetime as a function of $|\alpha|^2$ is largely independent of the particular Hamiltonian spectrum involved, provided the tunnel

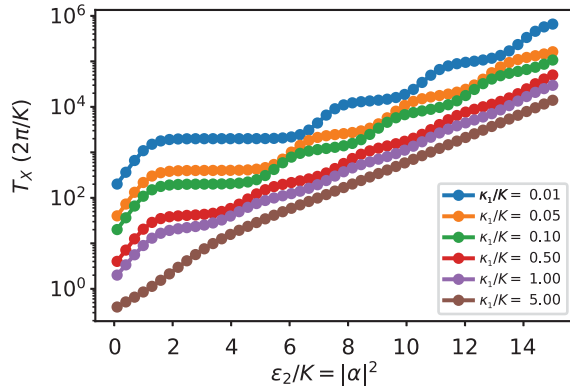


FIG. 14. The emergence of the Arrhenius law from quantum mechanics. As the dissipation overcomes the nonlinearity, the quantum features disappear, and the classical Arrhenius exponential law emerges from the staircase in T_X vs ϵ_2/K . The temperature was kept constant at $n_{\text{th}} = 0.05$. The interplay of macroscopicity, nonlinearity, and dissipation determines the quality of the classical treatment.

splitting vanishes for excited states progressively. This feature defines “double-well” potentials. This is a property strictly related to the “nonlocal” character of the phase-space double-well encoding in the classical limit $\epsilon_2 \gg K$.

Finally, in Fig. 14 we plot T_X against ϵ_2/K for different values of the single-photon-loss rate κ_1 . Note that, as explained in the main text, the location of the plateaus depends on κ_1 , illustrating the limitations of the naive Bohr quantization model. We see that, as the dissipation overcomes the nonlinearity, the quantum features disappear, and the classical Arrhenius exponential law emerges. This behavior is a generic feature of quantum mechanical double wells, and reflects the essence of the quantum to classical correspondence.

[1] W. H. Zurek, *Decoherence, einselection, and the quantum origins of the classical*, *Rev. Mod. Phys.* **75**, 715 (2003).
 [2] E. Merzbacher, *The early history of quantum tunneling*, *Phys. Today* **55**, No. 8, 44 (2002).
 [3] A. M. Steinberg, P. G. Kwiat, and R. Y. Chiao, *Measurement of the single-photon tunneling time*, *Phys. Rev. Lett.* **71**, 708 (1993).
 [4] J. R. Friedman, M. P. Sarachik, J. Tejada, and R. Ziolo, *Macroscopic measurement of resonant magnetization tunneling in high-spin molecules*, *Phys. Rev. Lett.* **76**, 3830 (1996).
 [5] A. I. Kolesnikov, G. F. Reiter, N. Choudhury, T. R. Prisk, E. Mamontov, A. Podlesnyak, G. Ehlers, A. G. Seel, D. J. Wesolowski, and L. M. Anovitz, *Quantum tunneling of water in beryl: A new state of the water molecule*, *Phys. Rev. Lett.* **116**, 167802 (2016).
 [6] D. DeVault, J. H. Parkes, and B. Chance, *Electron tunneling in cytochromes*, *Nature (London)* **215**, 642 (1967).

[7] M. H. Devoret, J. M. Martinis, and J. Clarke, *Measurements of macroscopic quantum tunneling out of the zero-voltage state of a current-biased Josephson junction*, *Phys. Rev. Lett.* **55**, 1908 (1985).
 [8] C. Spielmann, R. Szipöcs, A. Stingl, and F. Krausz, *Tunneling of optical pulses through photonic band gaps*, *Phys. Rev. Lett.* **73**, 2308 (1994).
 [9] P. Joyez, V. Bouchiat, D. Esteve, C. Urbina, and M. H. Devoret, *Strong tunneling in the single-electron transistor*, *Phys. Rev. Lett.* **79**, 1349 (1997).
 [10] A. Slobodskyy, C. Gould, T. Slobodskyy, C. R. Becker, G. Schmidt, and L. W. Molenkamp, *Voltage-controlled spin selection in a magnetic resonant tunneling diode*, *Phys. Rev. Lett.* **90**, 246601 (2003).
 [11] S. Fölling, S. Trotzky, P. Cheinet, M. Feld, R. Saers, A. Widera, T. Müller, and I. Bloch, *Direct observation of second-order atom tunnelling*, *Nature (London)* **448**, 1029 (2007).
 [12] E. Kierig, U. Schnorrberger, A. Schietinger, J. Tomkovic, and M. K. Oberthaler, *Single-particle tunneling in strongly driven double-well potentials*, *Phys. Rev. Lett.* **100**, 190405 (2008).
 [13] W. S. Bakr, J. I. Gillen, A. Peng, S. Fölling, and M. Greiner, *A quantum gas microscope for detecting single atoms in a Hubbard-regime optical lattice*, *Nature (London)* **462**, 74 (2009).
 [14] R. Ma, M. E. Tai, P. M. Preiss, W. S. Bakr, J. Simon, and M. Greiner, *Photon-assisted tunneling in a biased strongly correlated Bose gas*, *Phys. Rev. Lett.* **107**, 095301 (2011).
 [15] I. Bloch, J. Dalibard, and S. Nascimbène, *Quantum simulations with ultracold quantum gases*, *Nat. Phys.* **8**, 267 (2012).
 [16] M. Aidelsburger, M. Atala, M. Lohse, J. T. Barreiro, B. Paredes, and I. Bloch, *Realization of the Hofstadter Hamiltonian with ultracold atoms in optical lattices*, *Phys. Rev. Lett.* **111**, 185301 (2013).
 [17] A. Kaufman, B. Lester, C. Reynolds, M. Wall, M. Foss-Feig, K. Hazzard, A. Rey, and C. Regal, *Two-particle quantum interference in tunnel-coupled optical tweezers*, *Science* **345**, 306 (2014).
 [18] A. Noguchi, Y. Shikano, K. Toyoda, and S. Urabe, *Aharonov–Bohm effect in the tunnelling of a quantum rotor in a linear Paul trap*, *Nat. Commun.* **5**, 1 (2014).
 [19] A. Mazurenko, C. S. Chiu, G. Ji, M. F. Parsons, M. Kanász-Nagy, R. Schmidt, F. Grusdt, E. Demler, D. Greif, and M. Greiner, *A cold-atom Fermi–Hubbard antiferromagnet*, *Nature (London)* **545**, 462 (2017).
 [20] H. Zheng, J. Zhang, and R. Berndt, *A minimal double quantum dot*, *Sci. Rep.* **7**, 10764 (2017).
 [21] F. Schäfer, T. Fukuhara, S. Sugawa, Y. Takasu, and Y. Takahashi, *Tools for quantum simulation with ultracold atoms in optical lattices*, *Nat. Rev. Phys.* **2**, 411 (2020).
 [22] K. Wintersperger, C. Braun, F. N. Únal, A. Eckardt, M. Di Liberto, N. Goldman, I. Bloch, and M. Aidelsburger, *Realization of an anomalous Floquet topological system with ultracold atoms*, *Nat. Phys.* **16**, 1058 (2020).
 [23] R. Ramos, D. Spierings, I. Racicot, and A. M. Steinberg, *Measurement of the time spent by a tunnelling atom within the barrier region*, *Nature (London)* **583**, 529 (2020).

- [24] T.-K. Hsiao, C. J. van Diepen, U. Mukhopadhyay, C. Reichl, W. Wegscheider, and L. M. K. Vandersypen, *Efficient orthogonal control of tunnel couplings in a quantum dot array*, *Phys. Rev. Appl.* **13**, 054018 (2020).
- [25] N. Bohr and J. A. Wheeler, *The mechanism of nuclear fission*, *Phys. Rev.* **56**, 426 (1939).
- [26] E. Wigner, *On the quantum correction for thermodynamic equilibrium*, *Phys. Rev.* **40**, 749 (1932).
- [27] H. A. Kramers, *Brownian motion in a field of force and the diffusion model of chemical reactions*, *Physica (Amsterdam)* **7A**, 284 (1940).
- [28] A. Larkin and Y. N. Ovchinnikov, *Quantum-mechanical tunneling with dissipation: the pre-exponential factor*, *Zh. Eksp. Teor. Fiz.* **86**, 726 (1984).
- [29] M. Marthaler and M. I. Dykman, *Switching via quantum activation: A parametrically modulated oscillator*, *Phys. Rev. A* **73**, 042108 (2006).
- [30] M. I. Dykman, M. Marthaler, and V. Peano, *Quantum heating of a parametrically modulated oscillator: Spectral signatures*, *Phys. Rev. A* **83**, 052115 (2011).
- [31] J. E. Mooij, T. P. Orlando, L. Levitov, L. Tian, C. H. v. d. Wal, and S. Lloyd, *Josephson Persistent-current qubit*, *Science* **285**, 1036 (1999).
- [32] C. H. v. d. Wal, A. C. J. t. Haar, F. K. Wilhelm, R. N. Schouten, C. J. P. M. Harmans, T. P. Orlando, S. Lloyd, and J. E. Mooij, *Quantum superposition of macroscopic persistent-current states*, *Science* **290**, 773 (2000).
- [33] R. Rouse, S. Han, and J. E. Lukens, *Observation of resonant tunneling between macroscopically distinct quantum levels*, *Phys. Rev. Lett.* **75**, 1614 (1995).
- [34] S. Han, R. Rouse, and J. E. Lukens, *Generation of a population inversion between quantum states of a macroscopic variable*, *Phys. Rev. Lett.* **76**, 3404 (1996).
- [35] J. R. Friedman, V. Patel, W. Chen, S. K. Tolpygo, and J. E. Lukens, *Quantum superposition of distinct macroscopic states*, *Nature (London)* **406**, 43 (2000).
- [36] D. M. Berns, M. S. Rudner, S. O. Valenzuela, K. K. Berggren, W. D. Oliver, L. S. Levitov, and T. P. Orlando, *Amplitude spectroscopy of a solid-state artificial atom*, *Nature (London)* **455**, 51 (2008).
- [37] A. J. Berkley, A. J. Przybysz, T. Lanting, R. Harris, N. Dickson, F. Altomare, M. H. Amin, P. Bunyk, C. Enderud, E. Hoskinson, M. W. Johnson, E. Ladizinsky, R. Neufeld, C. Rich, A. Y. Smirnov, E. Tolkacheva, S. Uchaikin, and A. B. Wilson, *Tunneling spectroscopy using a probe qubit*, *Phys. Rev. B* **87**, 020502(R) (2013).
- [38] F. G. Paauw, A. Fedorov, C. J. P. M. Harmans, and J. E. Mooij, *Tuning the gap of a superconducting flux qubit*, *Phys. Rev. Lett.* **102**, 090501 (2009).
- [39] S. Gustavsson, J. Bylander, F. Yan, W. D. Oliver, F. Yoshihara, and Y. Nakamura, *Noise correlations in a flux qubit with tunable tunnel coupling*, *Phys. Rev. B* **84**, 014525 (2011).
- [40] M. J. Schwarz, J. Goetz, Z. Jiang, T. Niemczyk, F. Deppe, A. Marx, and R. Gross, *Gradiometric flux qubits with a tunable gap*, *New J. Phys.* **15**, 045001 (2013).
- [41] S. Novikov, R. Hinkey, S. Disseler, J. I. Basham, T. Albash, A. Risinger, D. Ferguson, D. A. Lidar, and K. M. Zick, *Exploring more-coherent quantum annealing*, in *IEEE International Conference on Rebooting Computing (ICRC)*, McLean, VA, USA, 2018 (2018) pp. 1–7, [10.1109/ICRC.2018.8638625](https://doi.org/10.1109/ICRC.2018.8638625).
- [42] W. D. Oliver, Y. Yu, J. C. Lee, K. K. Berggren, L. S. Levitov, and T. P. Orlando, *Mach-Zehnder interferometry in a strongly driven superconducting qubit*, *Science* **310**, 1653 (2005).
- [43] J. O. Hirschfelder and E. Wigner, *Some quantum-mechanical considerations in the theory of reactions involving an activation energy*, *J. Chem. Phys.* **7**, 616 (1939).
- [44] J. H. Weiner, *Quantum rate theory for a symmetric double-well potential*, *J. Chem. Phys.* **68**, 2492 (1978).
- [45] P. Hänggi, P. Talkner, and M. Borkovec, *Reaction-rate theory: Fifty years after Kramers*, *Rev. Mod. Phys.* **62**, 251 (1990).
- [46] D. A. Garanin and E. M. Chudnovsky, *Thermally activated resonant magnetization tunneling in molecular magnets: Mn₁₂Ac and others*, *Phys. Rev. B* **56**, 11102 (1997).
- [47] J. R. Friedman, *Quantum tunneling and classical barrier reduction for a mesoscopic spin*, *Phys. Rev. B* **57**, 10291 (1998).
- [48] A. Grimm, N. E. Frattini, S. Puri, S. O. Mundhada, S. Touzard, M. Mirrahimi, S. M. Girvin, S. Shankar, and M. H. Devoret, *Stabilization and operation of a Kerr-cat qubit*, *Nature (London)* **584**, 205 (2020).
- [49] S. Puri, A. Grimm, P. Campagne-Ibarcq, A. Eickbusch, K. Noh, G. Roberts, L. Jiang, M. Mirrahimi, M. H. Devoret, and S. M. Girvin, *Stabilized cat in a driven nonlinear cavity: A fault-tolerant error syndrome detector*, *Phys. Rev. X* **9**, 041009 (2019).
- [50] J. Guillaud and M. Mirrahimi, *Repetition cat qubits for fault-tolerant quantum computation*, *Phys. Rev. X* **9**, 041053 (2019).
- [51] S. Puri, L. St-Jean, J. A. Gross, A. Grimm, N. E. Frattini, P. S. Iyer, A. Krishna, S. Touzard, L. Jiang, A. Blais, S. T. Flammia, and S. M. Girvin, *Bias-preserving gates with stabilized cat qubits*, *Sci. Adv.* **6**, eaay5901 (2020).
- [52] J. P. Bonilla Ataides, D. K. Tuckett, S. D. Bartlett, S. T. Flammia, and B. J. Brown, *The XZZX surface code*, *Nat. Commun.* **12**, 2172 (2021).
- [53] A. S. Darmawan, B. J. Brown, A. L. Grimsmo, D. K. Tuckett, and S. Puri, *Practical quantum error correction with the XZZX code and Kerr-cat qubits*, *PRX Quantum* **2**, 030345 (2021).
- [54] C. Chamberland, K. Noh, P. Arrangoiz-Arriola, E. T. Campbell, C. T. Hann, J. Iverson, H. Putterman, T. C. Bohdanowicz, S. T. Flammia, A. Keller, G. Refael, J. Preskill, L. Jiang, A. H. Safavi-Naeini, O. Painter, and F. G. S. L. Brandão, *Building a fault-tolerant quantum computer using concatenated cat codes*, *PRX Quantum* **3**, 010329 (2022).
- [55] W. Wustmann and V. Shumeiko, *Parametric effects in circuit quantum electrodynamics*, *Low Temp. Phys.* **45**, 848 (2019).
- [56] S. M. Girvin, *Circuit QED: Superconducting qubits coupled to microwave photons*, *Quantum machines: measurement and control of engineered quantum systems*, in *Proceedings of the 2011 Les Houches Summer School on Quantum Machines*, edited by M. H. Devoret, R. J. Schoelkopf, B. Huard, and L. F. Cugliandolo (Oxford University Press, New York, 2014).

- [57] N. Frattini, U. Vool, S. Shankar, A. Narla, K. Sliwa, and M. Devoret, *3-wave mixing Josephson dipole element*, *Appl. Phys. Lett.* **110**, 222603 (2017).
- [58] N. E. Frattini, V. V. Sivak, A. Lingenfelter, S. Shankar, and M. H. Devoret, *Optimizing the nonlinearity and dissipation of a SNAIL parametric amplifier for dynamic range*, *Phys. Rev. Appl.* **10**, 054020 (2018).
- [59] V. V. Sivak, N. E. Frattini, V. R. Joshi, A. Lingenfelter, S. Shankar, and M. H. Devoret, *Kerr-free three-wave mixing in superconducting quantum circuits*, *Phys. Rev. Appl.* **11**, 054060 (2019).
- [60] M. Mirrahimi, Z. Leghtas, V. V. Albert, S. Touzard, R. J. Schoelkopf, L. Jiang, and M. H. Devoret, *Dynamically protected cat-qubits: A new paradigm for universal quantum computation*, *New J. Phys.* **16**, 045014 (2014).
- [61] Z. Leghtas, S. Touzard, I. M. Pop, A. Kou, B. Vlastakis, A. Petrenko, K. M. Sliwa, A. Narla, S. Shankar, M. J. Hatridge *et al.*, *Confining the state of light to a quantum manifold by engineered two-photon loss*, *Science* **347**, 853 (2015).
- [62] S. Touzard, A. Grimm, Z. Leghtas, S. O. Mundhada, P. Reinhold, C. Axline, M. Reagor, K. Chou, J. Blumoff, K. M. Sliwa, S. Shankar, L. Frunzio, R. J. Schoelkopf, M. Mirrahimi, and M. H. Devoret, *Coherent oscillations inside a quantum manifold stabilized by dissipation*, *Phys. Rev. X* **8**, 021005 (2018).
- [63] R. Lescanne, M. Villiers, T. Peronnin, A. Sarlette, M. Delbecq, B. Huard, T. Kontos, M. Mirrahimi, and Z. Leghtas, *Exponential suppression of bit-flips in a qubit encoded in an oscillator*, *Nat. Phys.* **16**, 509 (2020).
- [64] C. Berdou, A. Murani, U. Réglade, W. Smith, M. Villiers, J. Palomo, M. Rosticher, A. Denis, P. Morfin, M. Delbecq *et al.*, *One hundred second bit-flip time in a two-photon dissipative oscillator*, *PRX Quantum* **4**, 020350 (2023).
- [65] J. Venkatraman, X. Xiao, R. G. Cortiñas, A. Eickbusch, and M. H. Devoret, *Static effective Hamiltonian of a rapidly driven nonlinear system*, *Phys. Rev. Lett.* **129**, 100601 (2022).
- [66] S. Harris, *Tunable optical parametric oscillators*, *Proc. IEEE* **57**, 2096 (1969).
- [67] G. J. Milburn and C. A. Holmes, *Quantum coherence and classical chaos in a pulsed parametric oscillator with a Kerr nonlinearity*, *Phys. Rev. A* **44**, 4704 (1991).
- [68] G. Y. Kryuchkyan and K. Kheruntsyan, *Exact quantum theory of a parametrically driven dissipative anharmonic oscillator*, *Opt. Commun.* **127**, 230 (1996).
- [69] P. T. Cochrane, G. J. Milburn, and W. J. Munro, *Macroscopically distinct quantum-superposition states as a bosonic code for amplitude damping*, *Phys. Rev. A* **59**, 2631 (1999).
- [70] B. Wielinga and G. J. Milburn, *Quantum tunneling in a Kerr medium with parametric pumping*, *Phys. Rev. A* **48**, 2494 (1993).
- [71] C. M. Wilson, T. Duty, M. Sandberg, F. Persson, V. Shumeiko, and P. Delsing, *Photon generation in an electromagnetic cavity with a time-dependent boundary*, *Phys. Rev. Lett.* **105**, 233907 (2010).
- [72] V. Peano, M. Marthaler, and M. I. Dykman, *Sharp tunneling peaks in a parametric oscillator: Quantum resonances missing in the rotating wave approximation*, *Phys. Rev. Lett.* **109**, 090401 (2012).
- [73] H. Goto, *Bifurcation-based adiabatic quantum computation with a nonlinear oscillator network*, *Sci. Rep.* **6**, 21686 (2016).
- [74] Y. Zhang and M. I. Dykman, *Preparing quasienergy states on demand: A parametric oscillator*, *Phys. Rev. A* **95**, 053841 (2017).
- [75] S. Puri, S. Boutin, and A. Blais, *Engineering the quantum states of light in a Kerr-nonlinear resonator by two-photon driving*, *npj Quantum Inf.* **3**, 1 (2017).
- [76] H. Goto, *Quantum computation based on quantum adiabatic bifurcations of Kerr-nonlinear parametric oscillators*, *J. Phys. Soc. Jpn.* **88**, 061015 (2019).
- [77] Z. Wang, M. Pechal, E. A. Wollack, P. Arrangoiz-Arriola, M. Gao, N. R. Lee, and A. H. Safavi-Naeini, *Quantum dynamics of a few-photon parametric oscillator*, *Phys. Rev. X* **9**, 021049 (2019).
- [78] I. Strandberg, G. Johansson, and F. Quijandría, *Wigner negativity in the steady-state output of a Kerr parametric oscillator*, *Phys. Rev. Res.* **3**, 023041 (2021).
- [79] Q. Xu, J. K. Iverson, F. G. S. L. Brandão, and L. Jiang, *Engineering fast bias-preserving gates on stabilized cat qubits*, *Phys. Rev. Res.* **4**, 013082 (2022).
- [80] G. Margiani, S. Guerrero, T. L. Heugel, C. Marty, R. Pachlatko, T. Gisler, G. D. Vukasin, H.-K. Kwon, J. M. L. Miller, N. E. Bousse, T. W. Kenny, O. Zilberberg, D. Sabonis, and A. Eichler, *Extracting the lifetime of a synthetic two-level system*, *Appl. Phys. Lett.* **121**, 164101 (2022).
- [81] S. Masuda, T. Ishikawa, Y. Matsuzaki, and S. Kawabata, *Controls of a superconducting quantum parametron under a strong pump field*, *Sci. Rep.* **11**, 11459 (2021).
- [82] T. Yamaji, S. Kagami, A. Yamaguchi, T. Satoh, K. Koshino, H. Goto, Z. R. Lin, Y. Nakamura, and T. Yamamoto, *Spectroscopic observation of the crossover from a classical Duffing oscillator to a Kerr parametric oscillator*, *Phys. Rev. A* **105**, 023519 (2022).
- [83] K. Matsumoto, A. Yamaguchi, T. Yamamoto, S. Kawabata, and Y. Matsuzaki, *Spectroscopic estimation of the photon number for superconducting Kerr parametric oscillators*, *Jpn. J. Appl. Phys.* **62**, SC1097 (2023).
- [84] Y. Suzuki, S. Watabe, S. Kawabata, and S. Masuda, *Measurement-based state preparation of Kerr parametric oscillators*, [arXiv:2208.04542](https://arxiv.org/abs/2208.04542).
- [85] S. Masuda, T. Kanao, H. Goto, Y. Matsuzaki, T. Ishikawa, and S. Kawabata, *Fast tunable coupling scheme of Kerr-nonlinear parametric oscillators based on shortcuts to adiabaticity*, *Phys. Rev. Appl.* **18**, 034076 (2022).
- [86] R. Miyazaki, *Effective spin models of Kerr-nonlinear parametric oscillators for quantum annealing*, *Phys. Rev. A* **105**, 062457 (2022).
- [87] S. Kwon, S. Watabe, and J.-S. Tsai, *Autonomous quantum error correction in a four-photon Kerr parametric oscillator*, *npj Quantum Inf.* **8**, 40 (2022).
- [88] N. E. Frattini, *Three-wave mixing in superconducting circuits: Stabilizing cats with SNAILs*, Ph.D thesis, Yale University, 2021.
- [89] M. Hillery, R. O'Connell, M. Scully, and E. Wigner, *Distribution functions in physics: Fundamentals*, *Phys. Rep.* **106**, 121 (1984).
- [90] T. L. Curtright, D. B. Fairlie, and C. K. Zachos, *A Concise Treatise on Quantum Mechanics in Phase*

- Space* (World Scientific Publishing Company, Singapore, 2013).
- [91] F. Minganti, N. Bartolo, J. Lolli, W. Casteels, and C. Ciuti, *Exact results for Schrödinger cats in driven-dissipative systems and their feedback control*, *Sci. Rep.* **6**, 1 (2016).
- [92] H. Putterman, J. Iverson, Q. Xu, L. Jiang, O. Painter, F. G. S. L. Brandão, and K. Noh, *Stabilizing a bosonic qubit using colored dissipation*, *Phys. Rev. Lett.* **128**, 110502 (2022).
- [93] R. Gautier, A. Sarlette, and M. Mirrahimi, *Combined dissipative and Hamiltonian confinement of cat qubits*, *PRX Quantum* **3**, 020339 (2022).
- [94] Note that for the excited states, a photon-loss event \hat{a} creates excitations. This phenomenon is known as quantum heating [29].
- [95] Note that for much smaller values of κ_1/K , the RWA Lindbladian condition $\delta_n < \kappa_1$ will appreciably differ from the oversimplified Bohr quantization model.
- [96] S. T. Adams, E. H. da Silva Neto, S. Datta, J. F. Ware, C. Lampropoulos, G. Christou, Y. Myasoedov, E. Zeldov, and J. R. Friedman, *Geometric-phase interference in a Mn₁₂ single-molecule magnet with fourfold rotational symmetry*, *Phys. Rev. Lett.* **110**, 087205 (2013).
- [97] R. W. Alexander, A. E. Hughes, and A. J. Sievers, *Far-infrared properties of lattice resonant modes. III. Temperature effects*, *Phys. Rev. B* **1**, 1563 (1970).
- [98] M. I. Dykman and M. A. Krivoglaz, *Spectral distribution of nonlinear oscillators with nonlinear friction due to a medium*, *Phys. Status Solidi B* **68**, 111 (1975).
- [99] A. Petrescu, M. Malekakhlagh, and H. E. Türeci, *Lifetime renormalization of driven weakly anharmonic superconducting qubits. II. The readout problem*, *Phys. Rev. B* **101**, 134510 (2020).
- [100] M. Marthaler and M. I. Dykman, *Quantum interference in the classically forbidden region: A parametric oscillator*, *Phys. Rev. A* **76**, 010102(R) (2007).
- [101] D. Roberts and A. A. Clerk, *Driven-dissipative quantum Kerr resonators: New exact solutions, photon blockade and quantum bistability*, *Phys. Rev. X* **10**, 021022 (2020).
- [102] J. Venkatraman, R. G. Cortiñas, N. E. Frattini, X. Xiao, and M. H. Devoret, *A driven Kerr oscillator with two-fold degeneracies for qubit protection*, *Proc. Natl. Acad. Sci. U.S.A.* **121**, e2311241121 (2024).
- [103] D. Ruiz, R. Gautier, J. Guillaud, and M. Mirrahimi, *Two-photon driven Kerr quantum oscillator with multiple spectral degeneracies*, *Phys. Rev. A* **107**, 042407 (2023).
- [104] L. Gravina, F. Minganti, and V. Savona, *Critical Schrödinger cat qubit*, *PRX Quantum* **4**, 020337 (2023).
- [105] P. W. Shor, *Scheme for reducing decoherence in quantum computer memory*, *Phys. Rev. A* **52**, R2493 (1995).
- [106] Z. Chen *et al.* (Google Quantum AI), *Exponential suppression of bit or phase errors with cyclic error correction*, *Nature (London)* **595**, 383 (2021).
- [107] P. Campagne-Ibarcq, A. Eickbusch, S. Touzard, E. Zalys-Geller, N. E. Frattini, V. V. Sivak, P. Reinhold, S. Puri, S. Shankar, R. J. Schoelkopf, L. Frunzio, M. Mirrahimi, and M. H. Devoret, *Quantum error correction of a qubit encoded in grid states of an oscillator*, *Nature (London)* **584**, 368 (2020).
- [108] A. L. Grimsmo and S. Puri, *Quantum error correction with the Gottesman-Kitaev-Preskill code*, *PRX Quantum* **2**, 020101 (2021).
- [109] Q. Xu, J. K. Iverson, F. G. S. L. Brandão, and L. Jiang, *Engineering fast bias-preserving gates on stabilized cat qubits*, *Phys. Rev. Res.* **4**, 013082 (2022).
- [110] T. Kanao, S. Masuda, S. Kawabata, and H. Goto, *Quantum gate for a Kerr nonlinear parametric oscillator using effective excited states*, *Phys. Rev. Appl.* **18**, 014019 (2022).
- [111] H. Chono, T. Kanao, and H. Goto, *Two-qubit gate using conditional driving for highly detuned Kerr nonlinear parametric oscillators*, *Phys. Rev. Res.* **4**, 043054 (2022).
- [112] C. M. Wilson, G. Johansson, A. Pourkabirian, M. Simoen, J. R. Johansson, T. Duty, F. Nori, and P. Delsing, *Observation of the dynamical Casimir effect in a superconducting circuit*, *Nature (London)* **479**, 376 (2011).
- [113] M. Dykman, *Fluctuating Nonlinear Oscillators: From Nanomechanics to Quantum Superconducting Circuits* (Oxford, New York, 2012).
- [114] M. Caprio, P. Cejnar, and F. Iachello, *Excited state quantum phase transitions in many-body systems*, *Ann. Phys. (Amsterdam)* **323**, 1106 (2008).
- [115] P. Ribeiro, J. Vidal, and R. Mosseri, *Exact spectrum of the Lipkin-Meshkov-Glick model in the thermodynamic limit and finite-size corrections*, *Phys. Rev. E* **78**, 021106 (2008).
- [116] J. Chávez-Carlos, T. L. M. Lezama, R. G. Cortiñas, J. Venkatraman, M. H. Devoret, V. S. Batista, F. Pérez-Bernal, and L. F. Santos, *Spectral kissing and its dynamical consequences in the squeeze-driven Kerr oscillator*, *npj Quantum Inf.* **9**, 1 (2023).
- [117] I. Carusotto and C. Ciuti, *Quantum fluids of light*, *Rev. Mod. Phys.* **85**, 299 (2013).
- [118] Z. Wang, A. Marandi, K. Wen, R. L. Byer, and Y. Yamamoto, *Coherent Ising machine based on degenerate optical parametric oscillators*, *Phys. Rev. A* **88**, 063853 (2013).
- [119] S. Puri, C. K. Andersen, A. L. Grimsmo, and A. Blais, *Quantum annealing with all-to-all connected nonlinear oscillators*, *Nat. Commun.* **8**, 15785 (2017).
- [120] H. Goto and T. Kanao, *Chaos in coupled Kerr-nonlinear parametric oscillators*, *Phys. Rev. Res.* **3**, 043196 (2021).
- [121] D. Monteoliva and J. P. Paz, *Decoherence and the rate of entropy production in chaotic quantum systems*, *Phys. Rev. Lett.* **85**, 3373 (2000).
- [122] S. Habib, K. Shizume, and W. H. Zurek, *Decoherence, chaos, and the correspondence principle*, *Phys. Rev. Lett.* **80**, 4361 (1998).
- [123] S. E. Nigg, H. Paik, B. Vlastakis, G. Kirchmair, S. Shankar, L. Frunzio, M. H. Devoret, R. J. Schoelkopf, and S. M. Girvin, *Black-box superconducting circuit quantization*, *Phys. Rev. Lett.* **108**, 240502 (2012).
- [124] Z. K. Mineev, Z. Leghtas, S. O. Mundhada, L. Christakis, I. M. Pop, and M. H. Devoret, *Energy-participation quantization of Josephson circuits*, [arXiv:2010.00620](https://arxiv.org/abs/2010.00620).
- [125] C. Axline, M. Reagor, R. Heeres, P. Reinhold, C. Wang, K. Shain, W. Pfaff, Y. Chu, L. Frunzio, and R. J. Schoelkopf, *An architecture for integrating planar and 3D cQED devices*, *Appl. Phys. Lett.* **109**, 042601 (2016).

- [126] N. Didier, J. Bourassa, and A. Blais, *Fast quantum nondemolition readout by parametric modulation of longitudinal qubit-oscillator interaction*, *Phys. Rev. Lett.* **115**, 203601 (2015).
- [127] S. Touzard, A. Kou, N. E. Frattini, V. V. Sivak, S. Puri, A. Grimm, L. Frunzio, S. Shankar, and M. H. Devoret, *Gated conditional displacement readout of superconducting qubits*, *Phys. Rev. Lett.* **122**, 080502 (2019).
- [128] P. Campagne-Ibarcq, P. Six, L. Bretheau, A. Sarlette, M. Mirrahimi, P. Rouchon, and B. Huard, *Observing quantum state diffusion by heterodyne detection of fluorescence*, *Phys. Rev. X* **6**, 011002 (2016).
- [129] W. Pfaff, C. J. Axline, L. D. Burkhardt, U. Vool, P. Reinhold, L. Frunzio, L. Jiang, M. H. Devoret, and R. J. Schoelkopf, *Controlled release of multiphoton quantum states from a microwave cavity memory*, *Nat. Phys.* **13**, 882 (2017).
- [130] D. Sank, Z. Chen, M. Khezri, J. Kelly, R. Barends, B. Campbell, Y. Chen, B. Chiaro, A. Dunsworth, A. Fowler *et al.*, *Measurement-induced state transitions in a superconducting qubit: Beyond the rotating wave approximation*, *Phys. Rev. Lett.* **117**, 190503 (2016).
- [131] Z. K. Mineev, S. O. Mundhada, S. Shankar, P. Reinhold, R. Gutiérrez-Jáuregui, R. J. Schoelkopf, M. Mirrahimi, H. J. Carmichael, and M. H. Devoret, *To catch and reverse a quantum jump mid-flight*, *Nature (London)* **570**, 200 (2019).
- [132] R. Lescanne, L. Verney, Q. Ficheux, M. H. Devoret, B. Huard, M. Mirrahimi, and Z. Leghtas, *Escape of a driven quantum Josephson circuit into unconfined states*, *Phys. Rev. Appl.* **11**, 014030 (2019).
- [133] N. H. McCoy, *On the function in quantum mechanics which corresponds to a given function in classical mechanics*, *Proc. Natl. Acad. Sci. U.S.A.* **18**, 674 (1932).
- [134] H. J. Groenewold, *On the principles of elementary quantum mechanics*, in *On the Principles of Elementary Quantum Mechanics* (Springer, New York, 1946), pp. 1–56.
- [135] J. E. Moyal, *Quantum mechanics as a statistical theory*, *Math. Proc. Cambridge Philos. Soc.* **45**, 99 (1949).
- [136] P. A. M. Dirac, *On the analogy between classical and quantum mechanics*, *Rev. Mod. Phys.* **17**, 195 (1945).
- [137] Note that the cat coherence times drop as $T_Z \sim 1/\bar{n}$, the interfringe distance decreases as $\sim 1/\sqrt{\bar{n}}$, and the maximal Rabi rate as determined by the gap scales as $\Delta_{\text{gap}} \sim \bar{n}$. Thus, the amount of coherent operation over the Schrödinger cat superposition during the state's lifetime grows as $\sqrt{\bar{n}}$.
- [138] S. Haroche and J.-M. Raimond, *Exploring the Quantum: Atoms, Cavities, and Photons* (Oxford University Press, New York, 2006).
- [139] B. Yurke and D. Stoler, *Generating quantum mechanical superpositions of macroscopically distinguishable states via amplitude dispersion*, *Phys. Rev. Lett.* **57**, 13 (1986).
- [140] M. Oliva and O. Steuernagel, *Quantum Kerr oscillators' evolution in phase space: Wigner current, symmetries, shear suppression, and special states*, *Phys. Rev. A* **99**, 032104 (2019).